International Journal of Plasticity 170 (2023) 103773

Contents lists available at ScienceDirect

International Journal of Plasticity

journal homepage: www.elsevier.com/locate/ijplas

A robust and efficient hybrid solver for crystal plasticity

Chris Hardie [a,*], Daniel J. Long [b], Eralp Demir [c], Edmund Tarleton [c], Fionn P.E. Dunne [b]

[a] UK Atomic Energy Authority, Culham Science Centre, Abingdon, Oxfordshire, OX14 3DB, UK
[b] Department of Materials, Imperial College London, London, SW7 2BY, UK
[c] Department of Engineering Science, University of Oxford, Parks Road, Oxford, OX1 3PJ, UK

ARTICLE INFO

Keywords:
B. Crystal plasticity
C. Finite element
B. Rate-dependent material
C. Numerical algorithms
B. Elastic-viscoplastic material

ABSTRACT

Conventional crystal plasticity (CP) solvers are based on a Newton-Raphson (NR) approach which use an initial guess for the free variables (often stress) to be solved. These solvers are limited by a finite interval of convergence and often fail when the free variable falls outside this interval. Solution failure results in the reduction of the time increment to be solved, thus convergence of the CP solver is a bottleneck which determines the computational cost of the simulation. The numerical stability of the slip law in its inverted form offers a solver that isn't vulnerable to poor pre-conditioning (initial guess) and can be used to progress to a solution from a stable starting point (i.e., from zero slip rate $\dot{\gamma}_{\mathrm{p}}^{k} = 0\ \mathrm{s}^{-1}$). In this paper, a novel formulation that enables the application of the slip law in its inverted form is introduced; this treats all slip systems as independent by approximating the Jacobian as a diagonal matrix, thus overcomes ill-defined and singular Jacobians associated with previous approaches. This scheme was demonstrated to offer superior robustness and convergence rate for a case with a single slip system, however the convergence rate for extreme cases with several active slip systems was relatively poor. Here, we introduce a novel 'hybrid scheme' that first uses the reverse scheme for the first stage of the solution, and then transitions to the forward scheme to complete the solution at a higher convergence rate. Several examples are given for pointwise calculations, followed by CPFEM simulations for FCC copper and HCP Zircaloy-4, which demonstrated solver performance in practise. The performance of simulations using the hybrid scheme was shown to require six to nine times fewer increments compared to the conventional forward scheme solver based on a free variable of stress and initial guess based on a fully elastic increment.

1. Introduction

The popularity of the crystal plasticity finite element method (CPFEM) is ever increasing as a tool to enhance our understanding and predictive capabilities of deformation mechanisms at the microstructural (crystalline) scale. The maturity of CPFEM models has enabled simulations to provide real engineering insights on component failure (Hardie et al., 2022; Lu et al., 2020; Zhao et al., 2019) and there is now considerable interest in incorporating such models into multiphysics predictive tools and digital twins (Roters et al., 2019). Development of a truly predictive model often requires accurately capturing the underlying physical mechanisms of deformation, which in many cases necessitate the use of highly non-linear models to correctly represent material behavior. Examples

* Corresponding author.
E-mail address: chris.hardie@ukaea.uk (C. Hardie).

https://doi.org/10.1016/j.ijplas.2023.103773
Received 2 August 2023; Received in revised form 26 September 2023;
Available online 7 October 2023

include the use of exponential based slip laws to accurately reproduce the strain rate sensitivity (Dunne et al., 2007; Kocks et al., 1975), simulation of crack propagation (Wilson and Dunne, 2019; Zhang et al., 2020) and the use of hardening laws as a function of strain gradients, which provides length-scale dependence linked to the presence of geometrically necessary dislocations (Dunne et al., 2007). Unfortunately, these highly non-linear material models are challenging to solve numerically and often require discretising the problem into relatively small time increments for implicit integration, thus making simulations computationally expensive or even impractical to solve. In such situations temptations arise to both reduce the size and complexity of the finite element model and simplify the non-linear material model, or even turn to an explicit formulation (Harewood and McHugh, 2007), which risks the accumulation of errors.

Much of the recent work in this field has focused on the development of spectral methods for crystal plasticity by implementation of fast Fourier transforms to solve equilibrium of periodic unit cells (Dadhich and Alankar, 2022; Lebensohn and Needleman, 2016). Although these can increase the computational efficiency of the equilibrium solution, their application is limited (e.g., in terms of boundary conditions and geometry discretization), and more importantly they do not address convergence failure of the inner loop for the pointwise crystal plasticity solution. The latter can dominate the maximum solvable time increment and be the primary bottleneck to simulation efficiency. Thus, improvement to the convergence behavior of crystal plasticity solvers can enhance the performance of simulations irrespective of the equilibrium solver. There have been a limited number of studies which directly compare the efficiency and accuracy of implicit and explicit crystal plasticity solvers (Dumoulin et al., 2009; Harewood and McHugh, 2007; Ling et al., 2005) and various conclusions of these studies imply that the model performance depends on the application, including both the material model and boundary conditions. The comparison between implicit and explicit approaches includes the study of several important parameters that characterise the nature of the analysis; these include the rate dependence of plastic slip and the presence of other non-linear behavior such as contact. The difficultly that arises when modeling near rate-independent or low rate sensitivity materials, lies in the determination of active slip systems, the calculation of slip increments and the potential non-uniqueness of the solution (Akpama et al., 2016). The modeling of low-rate sensitivity introduces numerical instability due to the binary nature of slip activation on potentially multiple slip systems in a single increment. This proves particularly challenging for finding a converged solution by the implicit method, as evident by an increase in CPU time for the solution of models with decreasing rate dependence (Harewood and McHugh, 2007).

Most implicit schemes in crystal plasticity are based on a Newton-Raphson (N-R) 'predictor-corrector' method, which are commonly implemented to minimise the error in stress (Dunne et al., 2007; Roters et al., 2010). It is recognized that the performance of the N-R scheme is dependent on the initial guess for the solution that is used to initiate the iterative solver (Akpama et al., 2016). Several authors have reported the use of an optimized calculation for initial guesses, line search algorithms (Mánik et al., 2022) and solving for sub-increments (McGinty, 2001; Vieira de Carvalho et al., 2022), which can add to solver robustness but increases computational time. It has been shown that superior stability is offered by the use of slip laws in their reverse (or inverted) form (i.e. shear stress, τ, as a function of plastic shear strain rate (slip rate), $\dot{\gamma}_p$: $\tau = f(\dot{\gamma}_p)$, which was first demonstrated by Cuitino and Ortiz (1993). Previous approaches that utilise the inverted slip law, use an error function based on slip system shear stresses and have been demonstrated using a continuous slip law based on the fraction of shear stress over the critical shear stress, τ_c, raised by a power. Not only is the Jacobian matrix of the error function comparatively large and thus computationally expensive to invert, but problems also arise when slip systems are relatively inactive. For continuous slip laws, all slip systems are considered active and low stressed slip systems have very small values for slip rate, and the inverse of these that appear in the Jacobian can return a 'floating-point overflow error'[1] (i.e. infinity) (Ling et al., 2005). For discontinuous slip laws, inactive slip systems are determined by the condition $\tau^k < \tau_c^k$ for each slip system k, which return zero strain rates and derivatives. In these cases, the Jacobian is often ill-conditioned or singular due to slip system interdependency and uninvertible using standard techniques (Miehe and Schröder, 2001). Previous studies have introduced algorithms to identify active slip systems to reduce the size of Jacobian (Cuitino and Ortiz, 1993), which may also improve or prevent the rank deficiency problem, however results are subject to the performance of such an algorithm and requires a code that can deal with variable size Jacobians.

This paper describes the challenges and limitations of solving crystal plasticity problems with slip laws in their conventional form (i.e., $\dot{\gamma}_p = f(\tau)$) and introduces a simple method based on the reverse form, which overcomes the limitations outlined above and provides a robust means for solving all crystal plasticity problems. The simplified method is easy to implement in existing CPFEM code, and it is immune from the problems associated with active slip system identification and Jacobian inversion described above. We first present new theory and provide demonstration of an alternative solver that uses a predictor-corrector scheme based on slip. We use material properties for copper, with a relatively low critical resolved shear stress of 1 MPa, which promotes the activation of multiple slip systems providing a difficult problem for demonstration. The enhanced numerical stability of this approach is first presented for a single slip system in one dimension for single and multiple time increments and then multiple slip systems in three dimensions. The convergence rate of the different approaches is discussed and a hybrid scheme solving for both slip initially followed by stress is proposed as an optimal solution. Finally, the application of the new scheme in a CPFEM framework is investigated for both FCC and HCP crystals and the improvement is demonstrated on a polycrystalline, cyclically loaded model with hardening based on plastic strain gradients and crack propagation.

[1] Infinity is returned when a value larger than that which can be represented by the assigned storage for a variable is returned. For an 8-byte (double precision) variable, the maximum number that can be represented is 1.7977×10^{308}.

2. Theory

The set of crystal plasticity variables and linking equations that are used to demonstrate the concepts in the present study are given in the schematics shown in Figs. 1 and 3. These figures each introduce two calculation loops, one which illustrates the process for solving stress ($\boldsymbol{\sigma}$) and strain tensors ($\boldsymbol{\varepsilon}$) in a system of multiple slip systems in three dimensions, and the other illustrating the process for solving scalar values of shear stresses (τ) and shear strains (γ) for a single slip system in one dimension. Whilst these indicate the fundamental linkage between stress and strains, for simplicity they omit the complexities related to the accurate kinematic formulation that accounts for the evolution of a deformed configuration, including stretch and rotation, in the form of multiplicative decomposition of elastic and plastic deformation gradients (Roters et al., 2010). As such, the theory here and results for pointwise calculations presented in Section 4 are based on solving for a specified velocity gradient ($\boldsymbol{L}$) for three dimensional problems or a specified shear strain rate ($\dot{\gamma}$) for one dimensional problems, with their elastic and plastic components decomposed additively. This approach is representative of the iterative solver in many implicit CPFEM schemes, with state variables capturing the full kinematics being updated explicitly at the end of each increment. The simulations presented in Section 5 demonstrate implementation of the developed solvers into a CPFEM framework, which included full kinematic formulation for large deformations and rotations.

For the three-dimensional procedure, the increment in true strain ($\boldsymbol{\Delta\varepsilon}$) is calculated assuming small deformation, by integrating the symmetric part of the velocity gradient over the time increment with duration (Δt):

$$\boldsymbol{\Delta\varepsilon} = \ \mathrm{sym}(\boldsymbol{L})\Delta t = \frac{1}{2}\left(\boldsymbol{L}+\boldsymbol{L}^{\mathrm{T}}\right)\Delta t \tag{1}$$

where the sym() function refers to the symmetric part of the argument. Eq. (1) holds for both elastic and plastic components of $\boldsymbol{\Delta\varepsilon}$ and $\boldsymbol{L}$, where subscripts e and p are used to differentiate between them. The Schmid tensors are used to project the shear strains on all slip systems in three dimensions, to give the plastic velocity gradient ($\boldsymbol{L}_{\mathrm{p}}$):

$$\boldsymbol{L}_{\mathrm{p}} = \sum_{k=1}^{Nsys} \dot{\gamma}_{\mathrm{p}}^{k}\boldsymbol{M}^{k} \tag{2}$$

where $\dot{\gamma}_{\mathrm{p}}^{k}$ is the plastic shear strain rate (slip rate) and $\boldsymbol{M}^{k}$ is the Schmid tensor for slip system k and the summation is over all *Nsys* slip systems. The Schmid tensor is defined by the tensor product of the slip direction ($\boldsymbol{s}$) and slip plane normal ($\boldsymbol{n}$) vectors:

$$\boldsymbol{M}^{k} = \widehat{\boldsymbol{s}^{k}} \otimes \widehat{\boldsymbol{n}^{k}} \tag{3}$$

Throughout this paper the operator: refers to a double dot product, the 'hat', $\widehat{\ }$, refers to the unit vector and $\otimes$ refers to a dyadic product.

For simplicity, we neglect evolution of a deformed configuration and assume additive decomposition of the elastic and plastic parts of $\boldsymbol{L}$:

$$\boldsymbol{L} = \boldsymbol{L}_{\mathrm{e}} + \ \boldsymbol{L}_{\mathrm{p}} \tag{4}$$

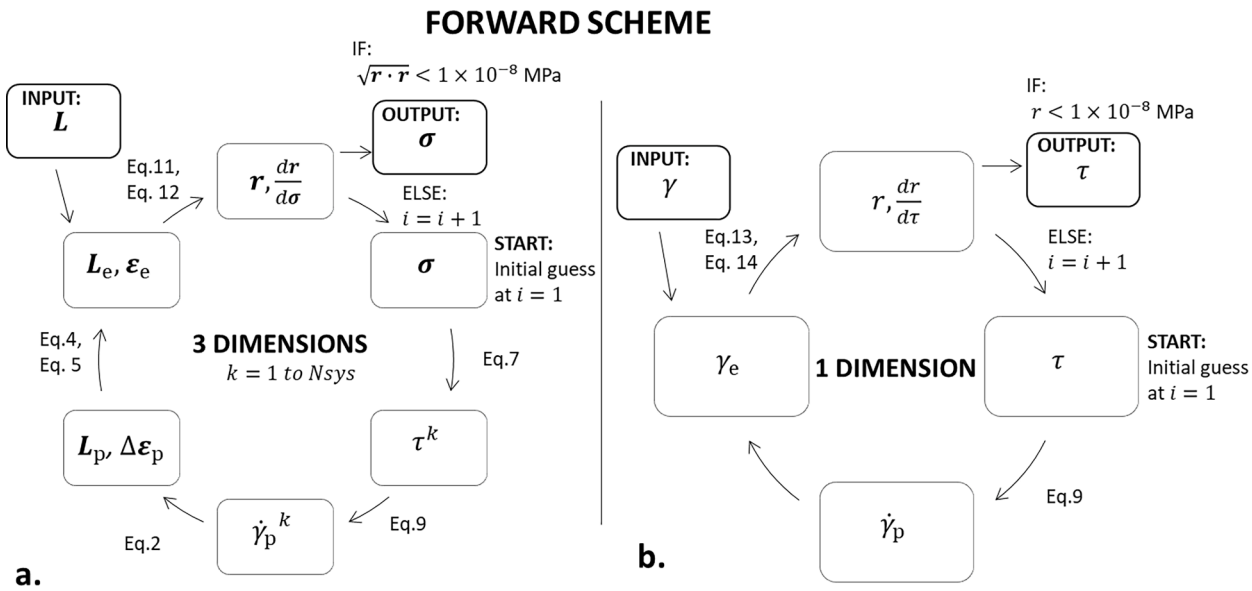

Fig. 1. Schematic showing the forward scheme calculation procedure and equation numbers used in this study for solving crystal plasticity problems in (a) 3 dimensions with multiple (*Nsys*) slip systems ($k = 1 : Nsys$) and (b) one dimension for a single slip system.

Therefore, strains are also treated additively and the increment in elastic strain is the total strain increment ($\boldsymbol{\Delta\varepsilon}$) minus the plastic strain increment, which is integrated over time, t, by:

$$\boldsymbol{\varepsilon}_{e(t+\Delta t)} = \boldsymbol{\varepsilon}_{e(t)} + \boldsymbol{\Delta\varepsilon} - \boldsymbol{\Delta\varepsilon}_p \tag{5}$$

where subscript (t) refers to the end of the previous increment and $(t+\Delta t)$ refers to the end of the current increment. The corresponding stress tensor is calculating using the fourth order elastic stiffness matrix, $\mathbb{C}$:

$$\boldsymbol{\sigma} = \mathbb{C} : \boldsymbol{\varepsilon}_e \tag{6}$$

For each slip system k the shear stress is calculated from the stress tensor using the same Schmid tensor defined in Eq. (3):

$$\tau^k = \boldsymbol{\sigma} : \boldsymbol{M}^k = \boldsymbol{M}^k : \boldsymbol{\sigma} \tag{7}$$

In this study, one-dimensional problems are based on a single slip system with scalar values of elastic and plastic shear strains which decompose additively. For one-dimensional problems, the geometrical description of slip systems in 3D by a Schmid tensor is not required, elasticity is simplified to a scalar value of shear modulus (G) and the equivalent of Eq. (6) is:

$$\tau = G\gamma_e \tag{8}$$

where γ_e is the elastic shear strain. The final linkage to complete the process illustrated in Fig. 1 is that between plastic slip rate and shear stress, which is often referred to as the slip law and is applicable to both three- and one-dimensional problems. The slip law is commonly defined as the plastic shear strain rate as a function of shear stress (and material properties) for a given slip system. The solver methods presented in this study are applicable to all slip laws and CP formulations. The aim of the present work is to demonstrate a robust approach to solving CP problems; thus, for demonstration with a particularly challenging case, we use the highly non-linear, exponential slip law where plastic shear strain rate is proportional to the hyperbolic sine of shear stress (Dunne et al., 2007):

$$\dot{\gamma}_p^k = \begin{cases} \alpha \sinh\left[\beta\left(\left|\tau^k\right| - \tau_c^k\right)\right] \mathrm{sgn}\left(\tau^k\right); & \text{for } \left|\tau^k\right| > \tau_c^k \\ 0; & \text{for } \left|\tau^k\right| \le \tau_c^k \end{cases} \tag{9}$$

Here α, and β are constants which are related to physically based material properties, sgn() is a function which returns the sign of the argument (i.e., this returns -1 if the argument is negative and +1 if the argument is positive), and $|\tau^k|$ signifies the absolute value of shear stress. Demonstration of the solver performances is also given in Appendix B for two other slip laws, namely the power type and enthalpy based slip law, which are commonly used in the literature.

For an arbitrary deformation, a CP solver must determine a single state of stress that satisfies the balance between the fraction of total deformation that is elastic and that which is plastic, where the rate form of the latter is a non-linear function of the stress. The non-linear relationship between stress and plastic strain rate requires solving the problem by use of an iterative approach, which in many cases involves a 'predictor-corrector' N-R algorithm based on an error function (as introduced below). Here the tangent (differential) of the error function for a given iteration i and guess, $x_{(i)}$, is used to extrapolate to zero error, r, for an improved guess, thereby approximating the system as linear at each iteration:

$$x_{(i+1)} = x_{(i)} - \left(\frac{dr_{(i)}}{dx_{(i)}}\right)^{-1} r_{(i)} \tag{10}$$

The N-R solver can be employed using an error function based on any of the variables shown in Fig. 1, however basing the scheme on the six independent components of stress is commonly preferred to minimise the dimensions of the Jacobian matrix (the derivative of the multidimensional error function) which requires inversion (Roters et al., 2010). The error function based on stress for the three-dimensional problem can thus take the form (Dunne et al., 2007):

$$\boldsymbol{r} = \mathbb{C} : (\boldsymbol{\varepsilon}_e + \boldsymbol{\Delta\varepsilon}) - \boldsymbol{\sigma} - \mathbb{C} : \boldsymbol{\Delta\varepsilon}_p = 0 \tag{11}$$

Eq. (11) and all error functions below are equated to zero on the right-hand side, which refers to the ideal solution (zero error). The derivative with respect to the stress guess is:

$$\frac{d\boldsymbol{r}}{d\boldsymbol{\sigma}} = -\left(\boldsymbol{I} + \mathbb{C} : \sum_{k=1}^{Nsys} \frac{d\dot{\gamma}_p^k}{d\tau^k} \mathrm{sym}\left(\boldsymbol{M}^k\right) \otimes \mathrm{sym}\left(\boldsymbol{M}^k\right) \Delta t\right) \tag{12}$$

Eqs. (11) and 12 are expressed in three-dimensional space, thus the error and its derivative are second order and fourth order tensors respectively. However, for numerical convenience, components of stress, strain and the Schmid tensor are commonly expressed as (6×1) vectors and the elastic stiffness matrix (6×6) matrix in Voigt notation.

For a one-dimensional problem the equivalent scalar error function is:

$$r = G(\gamma_e + \Delta\gamma) - \tau - G\dot{\gamma}_p \Delta t = 0 \tag{13}$$

and the derivative of this with respect to the shear stress guess is:

$$\frac{dr}{d\tau} = -\left(1 + G\frac{d\dot{\gamma}_p}{d\tau}\Delta t\right) \tag{14}$$

In the calculation of the error tangent, the derivative of the slip law with respect to shear stress is common to both one-dimensional and three-dimensional problems. For the slip law given in Eq. (9), its derivative is:

$$\frac{d\dot{\gamma}_p^k}{d\tau^k} = \alpha\beta\cosh\left[\beta\left(\left|\tau^k\right| - \tau_c^k\right)\right] \tag{15}$$

The solver algorithm for the forward scheme in three dimensions is shown in Box 1.

The limitation in the N-R scheme is the use of a linear tangent to calculate a new guess. The error functions in Eqs. (11) and (13) include linear components of elasticity (1D and 3D) and geometry (3D) and the non-linear slip law, the latter of which necessitates the use of the N-R approach and determines its performance. The non-linear part of the derivative in Eqs. (12) and (14) can be approximated as $Ae^{|\tau^k|}$ (where A is a constant), which produces a continuously increasing gradient with increase in shear stress. This is shown schematically for a one-dimensional problem in Fig. 2a, for a guess which is lower than that for the converged solution (superscript L, in red) and for a guess which is too high (superscript H, in blue). Here the cross at $r = 0$ represents the converged solution. As indicated for this case, if the guess is too high the tangent approximation underestimates the corrector, the error is reduced, and the algorithm iteratively progresses towards the solution in a stable fashion. However, if the guess is too low the tangent approximation overestimates the corrector and the following iteration overshoots and the error flips sign. The solver can fail to converge for two reasons, either the initial guess is too high and a floating-point overflow error arises or the initial guess is too low, leading to a stress corrector causing the same issue. It should be noted that for multidimensional problems, where there are multiple components of error (e.g., six components of stress), the tangent defined in Eq. (12) is in the form of a Jacobian matrix, which describes the interdependency between each component. The bounds of the derivative within this equation are $\alpha\beta|_{|\tau^k|=\tau_c^k} \leq \frac{d\dot{\gamma}_p^k}{d\tau^k} < \infty$, thus very large components within the Jacobian results in the matrix having a spectral range where the numerical precision of values is larger than the absolute value of other components, and the matrix effectively becomes ill-conditioned/singular (uninvertible using standard numerical techniques). In these instances, inversion using standard approaches (e.g. LU decomposition) is not possible and the solver fails, leading to a subsequent attempt with a cutback in the time increment.

The description above indicates that there is a finite range of values, the 'interval of convergence' in Fig. 2a, within which the initial guess successfully results in a converged solution using the N-R scheme in a clockwise fashion, as depicted in Fig. 1. For highly non-linear slip laws and materials with low strain rate sensitivity (higher values of β in the slip law used here), the interval of convergence is relatively narrow and making a successful initial guess particularly challenging; this frequently results in solution failure, cutbacks in increment time and is often the bottleneck which determines the computational demand for a given simulation. We now introduce a different scheme (hereafter referred to as the 'reverse scheme') based on calculating the non-linear part of this system in reverse, i.e., anticlockwise as shown in Fig. 3. Central to this is the re-arranged slip law (Eq. (9)) to give shear stress as a function of slip rate:

$$\tau_{vp}^k = \left[\tau_c^k + \beta^{-1}\sinh^{-1}\left(\frac{\left|\dot{\gamma}^k\right|}{\alpha}\right)\right]\mathrm{sgn}\left(\dot{\gamma}_p^k\right) \tag{16}$$

using $\mathrm{sgn}(\tau^k) = \mathrm{sgn}(\dot{\gamma}_p^k)$ and $|\tau^k| = \tau^k\mathrm{sgn}(\tau^k)$. The subscript 'vp' indicates that this value for shear stress has been calculated from the visco-plastic slip law as opposed to elasticity (Eq. (7)). The differential of this with respect to slip rate is:

Box 1
Forward Scheme Algorithm for each iteration, i

i. $\boldsymbol{\sigma}$ from initial guess at ($i = 1$) or $\boldsymbol{\sigma}_{(i+1)} = \boldsymbol{\sigma}_{(i)} + \left(\frac{d\boldsymbol{r}}{d\boldsymbol{\sigma}}\right)^{-1}_{(i)} \boldsymbol{r}_{(i)}$

ii. Slip system resolved shear stresses, τ^k from Eq. (7)
iii. Slip on each slip system, $\dot{\gamma}_p^k$ from Eq. (9)
iv. Plastic deformation, $\boldsymbol{L}_p$ from Eq. (2) and $\Delta\boldsymbol{\varepsilon}_p$
v. Elastic deformation, $\boldsymbol{\varepsilon}_{e(t+\Delta t)}$ from Eq. (5)
vi. Stress, $\boldsymbol{\sigma}$ from Eq. (6)
vii. Error and Jacobian, $\boldsymbol{r}$ and $\frac{d\boldsymbol{r}}{d\boldsymbol{\sigma}}$ from Eqs. (11) and (12)
viii. IF $\sqrt{\boldsymbol{r}\cdot\boldsymbol{r}} > tol$ go to step i

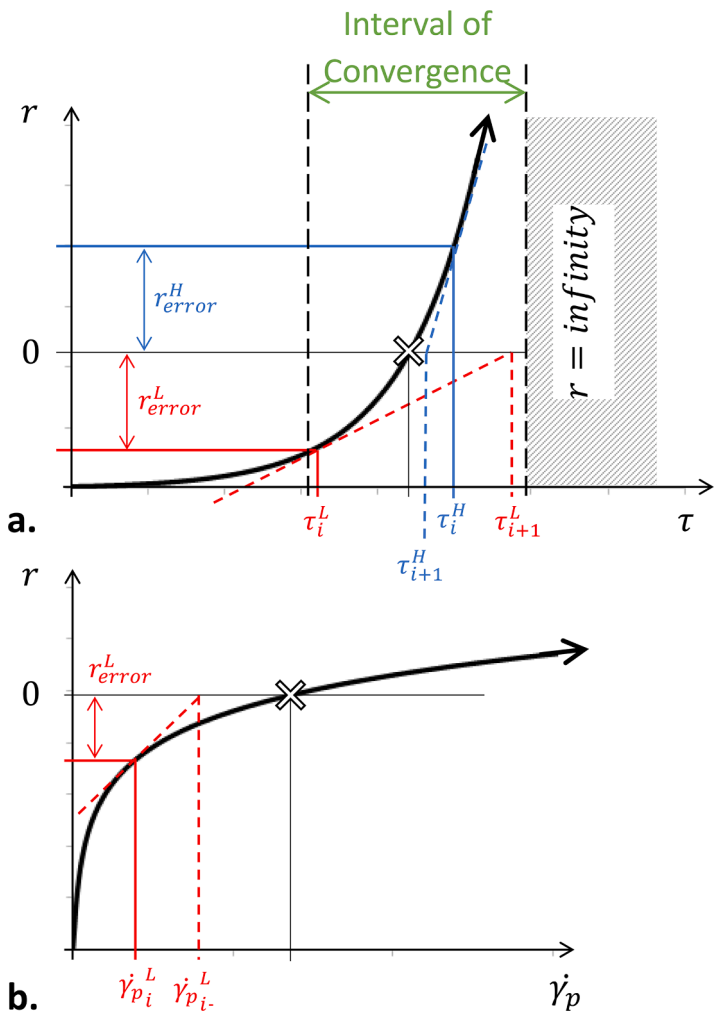

Fig. 2. Schematics showing (a) the tangents and corrections for a prediction of $\boldsymbol{\tau}$ lower than required and higher than required using the slip law in the form $\dot{\boldsymbol{\gamma}} = \boldsymbol{f}(\boldsymbol{\tau})$, and (b) the tangent and correction for a prediction of $\dot{\gamma}_p$ that is lower than required thus resulting in a stable correction of $\dot{\gamma}_p$ towards a converged solution using the reverse slip law ($\boldsymbol{\tau} = \boldsymbol{f}(\dot{\boldsymbol{\gamma}})$).

$$\frac{d\tau^k_{\mathrm{vp}}}{d\dot{\gamma}^k_{\mathrm{p}}} = \left[\alpha\beta\sqrt{\left(\frac{\dot{\gamma}^k_{\mathrm{p}}}{\alpha}\right)^2 + 1}\right]^{-1} \tag{17}$$

This rearrangement of the same non-linear problem enables a N-R scheme based on the slip rate on each slip system. Critically, this offers the possibility of a robust initial guess that all slip systems are inactive ($\dot{\gamma}^k_{\mathrm{p}} = 0\ \mathrm{s}^{-1}$), which results in a tangent that underestimates the change in slip rate (the corrector) and thus progresses towards the solution in a stable manner as depicted in Fig. 2b.

Using this reverse calculation and guess in slip rate, the derivative of the error function for the one-dimensional case (Eq. (13)) is:

$$\frac{dr}{d\dot{\gamma}_{\mathrm{p}}} = -\left(\frac{d\tau}{d\dot{\gamma}_{\mathrm{p}}} + G\Delta t\right) \tag{18}$$

Extending this reverse scheme to three-dimensional problems is less trivial due to the algebraic (geometrical) linear dependence of slip systems in three dimensions. Firstly, because of the linear dependence between slip systems, there is a non-unique set of *Nsys* slip system shear strains that can accommodate the five components of an arbitrary deviatoric strain (see Box. 2).

Box 2
Example of algebraic (geometrical) linear dependence between slip systems

The three <a> type slip systems which lie on the two-dimensional basal plane in HCP crystals provide a convenient example, these are linearly dependent because shear strain caused by the slip of one system could equally be accommodated by slip in the other two systems. This problem extends to all crystal structures with multiple slip systems, including the FCC structure investigated here.

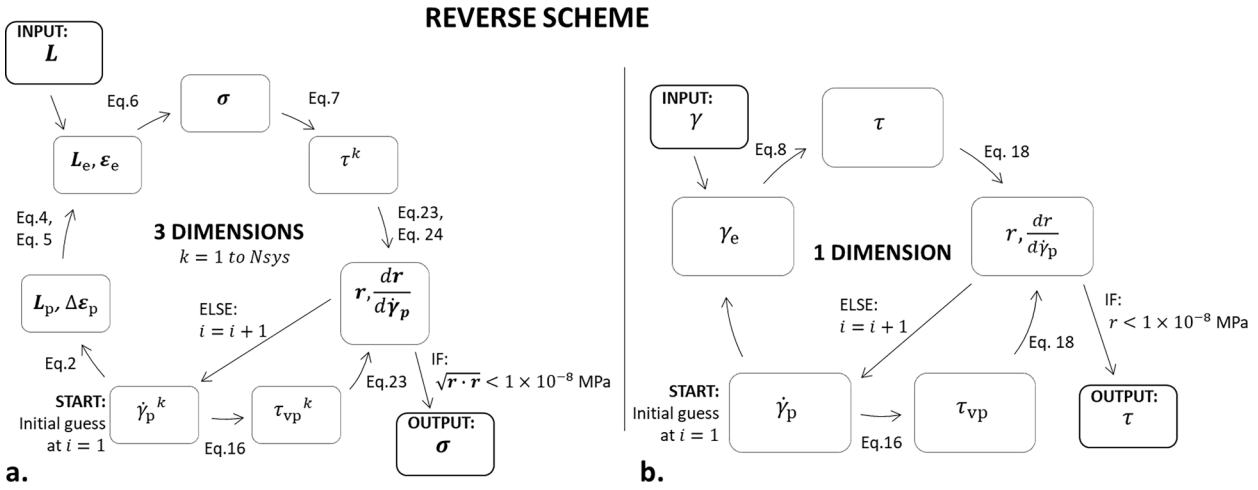

Fig. 3. Schematic showing the reverse scheme calculation procedure and equation numbers used in this study for solving crystal plasticity problems in (a) 3 dimensions with multiple (Nsys) slip systems (k=1:Nsys) and (b) one dimension for a single slip system.

This problem is well discussed in studies based on rate independent plasticity (Busso and Cailletaud, 2005), and the popularity of rate dependent crystal plasticity, in part, can be attributed to its provision of a unique selection of active slip systems (Peirce et al., 1983). Secondly, shear stresses on multiple slip systems are not linearly independent and must therefore satisfy equilibrium. They are a function of five independent components of deviatoric stress and therefore shear stresses on a maximum of only five slip systems can be algebraically linearly independent; however, as described above in Box 2, as few as three slip systems can be linearly dependent. Therefore, a N-R scheme with an error function based on tensorial plastic strain components (analogous to that based on stress in Eq. (11)) is not possible for the reverse scheme, since the rate dependence for each slip system is lost (due to dimension reduction by projecting *Nsys* components in $\mathbb{R}^6$ space) and equilibrium of shear stresses on multiple slip systems cannot be enforced. We therefore introduce a different error function for three-dimensional problems solved using the reverse scheme, based on shear stresses on all slip systems. From Eqs. (5)–(7), the shear stress for each slip system calculated from the elastic strain is:

$$\tau^k = \boldsymbol{M}^k : \mathbb{C} : \left(\boldsymbol{\varepsilon}_{e(t)} + \Delta\boldsymbol{\varepsilon} - \Delta\boldsymbol{\varepsilon}_p\right) \tag{19}$$

where $\boldsymbol{M}^k$ is the (3 × 3) Schmid tensor given in Eq. (3). Substituting the expression for $\Delta\boldsymbol{\varepsilon}_p$ in Eq. (2):

$$\tau^k = \boldsymbol{M}^k : \mathbb{C} : \left(\boldsymbol{\varepsilon}_{e(t)} + \Delta\boldsymbol{\varepsilon}\right) - \boldsymbol{M}^k : \mathbb{C} : \left(\sum_{l=1}^{Nsys} \boldsymbol{M}^l \dot{\gamma}_p^l \Delta t\right) \tag{20}$$

where we have removed the symmetry operation on $\boldsymbol{M}^l$ in Eq. (20), since it becomes redundant upon the double dot product with the elastic stiffness matrix which has minor symmetries (e.g., $\mathbb{C}_{ijkl} = \mathbb{C}_{ijlk}$). Finally, introducing the shear stresses and strain rates for all slip systems as *Nsys* × 1 vectors with symbols $\boldsymbol{\tau}$ and $\dot{\boldsymbol{\gamma}}$ respectively, we get a vectorised expression for shear stresses on all slip systems:

$$\tau^k = \boldsymbol{M}^k : \mathbb{C} : \left(\boldsymbol{\varepsilon}_{e(t)} + \Delta\boldsymbol{\varepsilon}\right) - G^{kl}\dot{\gamma}_p^l \Delta t \tag{21}$$

where G^{kl} are the components of the slip system elastic stiffness matrix with dimensions *Nsys* × *Nsys*:

$$G^{kl} = \boldsymbol{M}^k : \mathbb{C} : \boldsymbol{M}^l \tag{22}$$

For a converged solution the values for shear stress calculated using elasticity (Eq. (21)) and using visco-plasticity in Eq. (16) ($\boldsymbol{\tau}_{vp}$) must be equal, thus the following error function is defined:

$$\boldsymbol{r} = \boldsymbol{\tau} - \boldsymbol{\tau}_{\mathrm{vp}} = 0 \tag{23}$$

The derivative of the error function for the reverse scheme in three-dimensions is simply a vectorised version of the one-dimensional case:

$$\frac{d\boldsymbol{r}}{d\dot{\boldsymbol{\gamma}}_{\mathrm{p}}} = \frac{d\boldsymbol{\tau}}{d\dot{\boldsymbol{\gamma}}_{\mathrm{p}}} + \widetilde{\mathbb{G}}\Delta t \tag{24}$$

In contrast to the forward scheme described above the bounds of the derivative in Eq. (17) are $0|_{\dot{\gamma}_{\mathrm{p}}^k \to \infty} < \frac{d\tau^k}{d\dot{\gamma}_{\mathrm{p}}^k} \leq \frac{1}{\alpha\beta}|_{\dot{\gamma}_{\mathrm{p}}^k \to 0}$, thus the Jacobians calculated for the reverse scheme are not vulnerable to the spectral range problems described above for the forward scheme. In Eq. (22) G^{kl} is a fully populated matrix that captures the interdependencies between slip systems as described above, however this matrix is singular (with a maximum rank equal to five) due to interdependency between slip systems. For slip laws that express slip rate as a continuous function of shear stress, such as the power law form, all slip systems are assumed active and the first term on the RHS of Eq. (24) is non-zero on all slip systems; this adds additional values to the diagonal terms in G^{kl} resulting in an invertible, full rank matrix. However, the exponential based slip laws express slip rate as a non-continuous function of shear stress, restricted by the condition $|\tau^k| > \tau_{\mathrm{c}}^k$. Multiple slip systems remain inactive for many cases and the corresponding first term on the RHS of Eq. (24) is zero; this often results in a rank deficient (uninvertible) Jacobian or unstable performance. Here, we introduce $\widetilde{\mathbb{G}}$ as a diagonal matrix of independent shear moduli calculated for each slip system k by:

$$\widetilde{\mathbb{G}} = \left[\boldsymbol{M}^k : \mathbb{C} : \boldsymbol{M}^l\right]\delta^{kl} \tag{25}$$

where δ^{kl} is the Kronecker delta matrix ($Nsys \times Nsys$) with a value of one where $k = l$ and zero where $k \neq l$, thereby essentially omitting all off-diagonal components such that it has the form:

$$\widetilde{\mathbb{G}} = \begin{pmatrix} G^{11} & \cancelto{0}{G^{12}} & \dots & \cancelto{0}{G^{1Nsys}} \\ \cancelto{0}{G^{21}} & G^{22} & \dots & \cancelto{0}{G^{2Nsys}} \\ \vdots & \dots & \ddots & \vdots \\ \cancelto{0}{G^{Nsys1}} & \cancelto{0}{G^{Nsys2}} & \dots & G^{NsysNsys} \end{pmatrix} \tag{26}$$

This approximation is only used for the Jacobian. It provides correctors for slip rate based on $Nsys$ independent equations and calculation of its inverse is thus trivial, which is advantageous compared to the inversion of a non-diagonal $Nsys \times Nsys$ matrix. The removal of off-diagonal components effectively treats the corrector for each slip system independently and disregards the interdependency of the slip systems; this influences the rate of convergence, but it does not influence the converged solution. The errors for each slip system given by Eq. (23) are not subject to the approximation above and enforce the equality of shear stresses calculated by elasticity and visco-plasticity, and critically enforces equilibrium of the shear stresses due to interdependencies.

The loss of coefficients that represent the interdependency of slip systems can reduce the convergence rate and stability of the N-R loop when multiple interdependent slip systems are active. To overcome this the 'corrector' equation includes a step size or 'damping factor', ϕ, to ensure stability:

Box 3
Reverse Scheme Algorithm for each Iteration

i. Slip rate on each slip system, $\dot{\boldsymbol{\gamma}}_{\mathrm{p}}$ from initial guess (i.e., $\dot{\boldsymbol{\gamma}}_{\mathrm{p}} = 0.0\ s^{-1}$ at $i = 1$) or from Eq. (27)
ii. Slip system resolved shear stress, $\boldsymbol{\tau}$ calculated using elasticity from Eq. (21)
iii. IF $|\tau^k| > \tau_{\mathrm{c}}^k$ or $\left|\dot{\gamma}_{\mathrm{p}}^k\right| > 1 \times 10^{-6}\ s^{-1}$:

Slip system resolved shear stress, $\boldsymbol{\tau}_{\mathrm{vp}}$ calculated using viscoplasticity from Eq. (16)

ELSE

$$\tau_{\mathrm{vp}}^k = \tau^k$$

iv. Error and Jacobian, $\boldsymbol{r}$ and $\frac{d\boldsymbol{r}}{d\dot{\gamma}_{\mathrm{p}}}$ from Eqs. (23) and (24)
v. IF $\sqrt{\boldsymbol{r}\cdot\boldsymbol{r}} > tol$ go to step i

$$\dot{\boldsymbol{\gamma}}_{\mathrm{P}_{(i+1)}} = \dot{\boldsymbol{\gamma}}_{\mathrm{P}_{(i)}} - \phi\left(\frac{d\boldsymbol{r}_{(i)}}{d\dot{\boldsymbol{\gamma}}_{\mathrm{P}(i)}}\right)^{-1}\boldsymbol{r}_{(i)} \tag{27}$$

$$\phi = \min\left(\frac{\chi}{N_{act}}, 0.5\right) \tag{28}$$

where N_{act} is the number of active slip systems and χ is a constant to set the step size. For all later calculations on the FCC copper material in three dimensions and multiple slip systems, $\chi = 2.0$ was selected as a good compromise between solver stability and convergence rate. For all one-dimensional, single slip system calculations, Eq. (28) was not used and $\phi = 1.0$. The algorithm for the reverse scheme solver in three dimensions is shown in Box 3.

From step (iii) the components of error of non-active slip systems are equal to zero. The bound for $|\dot{\gamma}_{\mathrm{p}}^{k}|$ in step (iii) supports a smooth behavior by avoiding large jumps in slip rate associated with slip systems that transition from active to non-active during the solution.

For the three-dimensional calculations with multiple slips systems the norm of the error vector ($r = \sqrt{\boldsymbol{r}\cdot\boldsymbol{r}}$) is used as a convergence criterion metric. Throughout this study, a convergence criterion of $r < tol$ where $tol = 10^{-8}$ MPa for all schemes in one and three dimensions was used.

3. Methodology

The previous section outlines a simple CP formulation, the challenges in solving the non-linear problem and a new approach that was developed for improved stability. The following sections of the paper compare the different schemes by conducting a pointwise calculation using MATLAB®. Firstly, we compare the behavior of the forward and reverse schemes for a one-dimensional, single slip system by investigating the evolution of error as a function of iteration within a single increment, with different fractions of elastic and plastic strain. We then extend this study to demonstrate the multiple time increments required to solve these conditions for both a one-dimensional model with a single slip system and a three-dimensional model with multiple slip systems.

The schemes are compared by using pure copper as an example, with typical properties presented in Table 1 (Cackett et al., 2019). The slip system geometries, including the slip plane normal and slip directions are given in Appendix A.

The calculations in this study focus on three conditions of applied deformation rate. For a single slip system in one dimension, the following total shear strain rates were used:

(i) Condition A: $\dot{\gamma} = 3.29 \times 10^{-4}\ s^{-1}$
(ii) Condition B: $\dot{\gamma} = 1.44 \times 10^{-2}\ s^{-1}$
(iii) Condition C: $\dot{\gamma} = 1.36\ s^{-1}$

To extend these conditions to calculations in three dimensions an applied deformation rate was defined in the form of a velocity gradient. Uniaxial and shear loading types were investigated. For consistency with the one-dimensional conditions, the loading conditions were defined such that the slip rate on at least one of the slip systems closely matched that for the one-dimensional conditions. For the uniaxial type loading along axis 1, eight slip systems (1, 3, 4, 6, 7, 9, 10 & 12 as defined in Appendix A) are active and equally stressed. These slip systems can collectively accommodate a velocity gradient of the form:

$$\boldsymbol{L}_{\mathrm{UA}} = \sum_{k=1,3,4,6,7,9,10,12} \boldsymbol{M}^{k}\dot{\gamma}^{k} = \begin{pmatrix} 8a & 0 & 0 \\ 0 & -8b & 0 \\ 0 & 0 & -8b \end{pmatrix} \tag{29}$$

where $a = 0.4082\ s^{-1}$ and $b = a/2$ are the components of slip rate provided by each slip system in this specific case where eight slip systems are equally active. The value for a is found by multiplying the Schmid factor by the required slip for each condition (i.e., $a = 1/\sqrt{6}\ \dot{\gamma}^{k}$). Thus, for the uniaxial loading, the three conditions of applied deformation rate were:

(i) Condition A: $a = 1.343 \times 10^{-4}\ s^{-1}$
(ii) Condition B: $a = 5.9 \times 10^{-3}\ s^{-1}$

Table 1
Material properties and slip rate parameters for copper (Cackett et al., 2019).

Property	Symbol (s)	Value	Unit
Young's Modulus	E_{11}	66.69	GPa
Shear Modulus	G_{12}	75.4	GPa
Poisson's Ratio	ν_{12}	0.4189	
CRSS	τ_{c}	1.0	MPa
Slip rate parameter	α	5×10^{-5}	s^{-1}
Slip rate parameter	β	0.2	MPa^{-1}

(iii) Condition C: $a = 0.5552\ s^{-1}$

For the shear loading type, a velocity gradient which resulted in direct shearing of slip system 1 was defined. The Schmid tensor for slip system 1, with $\widehat{s^1} = [1\ \bar{1}\ 0]/\sqrt{2}$ and $\widehat{n^1} = [1\ 1\ 1]/\sqrt{3}$, is:

$$\boldsymbol{M}^1 = \begin{pmatrix} 0.4082 & 0.4082 & 0.4082 \\ -0.4082 & -0.4082 & -0.4082 \\ 0.0 & 0.0 & 0.0 \end{pmatrix} \tag{30}$$

This slip system accommodates a velocity gradient of the form:

$$\boldsymbol{L}_{S1} = \boldsymbol{M}^1 \dot{\gamma}^1 = \begin{pmatrix} a & a & a \\ -a & -a & -a \\ 0 & 0 & 0 \end{pmatrix} \tag{31}$$

where the values of a for three conditions of deformation rate defined for shear loading are the same as the three conditions (iv, v and vi) for the uniaxial loading conditions.

It should be noted that these conditions for applied loading in 3D were defined to closely match the 1D conditions, however the slip conditions between 1D and 3D are not identical due to the influence of Poisson's strains and the activation of multiple slip systems in the shear loading condition.

4. Results

4.1. Error evolution for a one-dimensional, single slip system within a single increment

In this section, simulations for a single slip system in one dimension were conducted starting from a relaxed system (zero initial strain), and solving for the three total shear strain rates, conditions A, B and C, over a single time increment of $\Delta t = 0.1$ s. To demonstrate the iterative behavior of each scheme, different fractions, θ, of the converged solution were used to initiate the N-R loop. For clarity, the initial guesses (τ_{guess}) for the forward scheme were calculated from the converged solution ($\tau_{\text{converged}}$) by $\tau_{\text{guess}} = \theta\tau_{\text{converged}}$, and the initial guess for the reverse scheme was calculated using the same method, $\dot{\gamma}_{\text{P}_{\text{guess}}} = \theta\dot{\gamma}_{\text{P}_{\text{converged}}}$. The fractions used were:

- Forward Scheme fractions, $\theta = 0.1, 0.5, 2.0, 10.0$
- Reverse Scheme fractions, $\theta = 0.0, 10.0, 50.0, 100.0$

For condition A, the converged solution returned an equilibrium stress of $\tau_{\text{converged}} = 1.33$ MPa and with a plastic shear strain rate ($\dot{\gamma}_{\text{P}_{\text{converged}}}$) 100 times lower than the specified total rate at $\Delta t = 0.1$ s (i.e., 99 % of the total deformation was elastic). The error residual as a function of N-R iterations for each case and both schemes are shown in Fig. 4a and b. The initial errors for guesses which underestimated stress in the forward scheme (i.e., for $\theta = 0.1$ and $\theta = 0.5$) were -1.2 MPa and -0.69 MPa respectively, with subsequent errors reducing in a stable manner to convergence in just three iterations. The error evolutions for these cases were entirely negative and therefore the data for these are not presented in Fig. 4a which has a logarithmic y-axis. For the initial guesses that overestimated the converged solution the initial errors were 1.38 MPa (for $\theta = 2.0$) and 13.13 MPa (for $\theta = 10.0$) which converged in three and four iterations respectively. The initial errors in the reverse scheme were -0.34, 2.88, 9.86 and 13.91 MPa for $\theta = 0.0,\ 10.0,\ 50.0$ and 100.0 respectively. The error reduced steadily to below the tolerance in just three iterations for $\theta = 0.0$, and four iterations for $\theta = 10.0$, however the error changed sign at each iteration for $\theta = 10.0$ and $\theta = 50.0$, which corresponded to the plastic shear strain changing sign at each iteration due to overshoot in the corrector. Error progressively reduced resulting in convergence in eight iterations for the $\theta = 50.0$ calculation, however error progressively increased for the largest initial guess and convergence was not achieved.

For condition B, the converged solution returned an equilibrium shear stress of $\tau_{\text{converged}} = 29.3$ MPa, which is far higher than condition A due to the increased viscoplastic response at this higher strain rate. The error residual as a function of N-R iterations for each case and both schemes are shown in Fig. 4c and d. For this condition all values of initial guess resulted in a converged solution. Overestimating the initial guess by a factor of $\theta = 10$ resulted in an initial error larger than 10^{24} MPa in the forward scheme, which illustrates the explosive nature of the sinh() function in the slip law. Despite this, the error progressively reduced with each iteration resulting in convergence after 58 iterations. Overestimating the initial guess by a factor of $\theta = 2$ resulted in an initial error of $\sim 10^4$ MPa, which also progressively reduced and converged within 11 iterations. Underestimating the initial guess produces initial errors which are negative and instantly lead to an over prediction of stress, resulting in errors on the 2$^{\text{nd}}$ iteration of $> 2 \times 10^3$ MPa (for $\theta = 0.1$) and ~ 980 MPa (for $\theta = 0.5$), with the solution reaching convergence with 12 and 10 iterations respectively. The initial errors in the calculations using the reverse scheme were -57.6, 276, 1460 and 2930 MPa for values of θ of 0, 10, 50 and 100 respectively. The positive errors associated with initial guesses that overestimated the slip rate had a negative error on the second iteration and all calculations converged within seven or fewer iterations.

For the most extreme total shear strain rate defined by condition C, the converged solution returned an equilibrium shear stress of $\tau_{\text{converged}} = 55.47$ MPa which again is higher than previous conditions due to the higher strain rate. The error residual as a function of

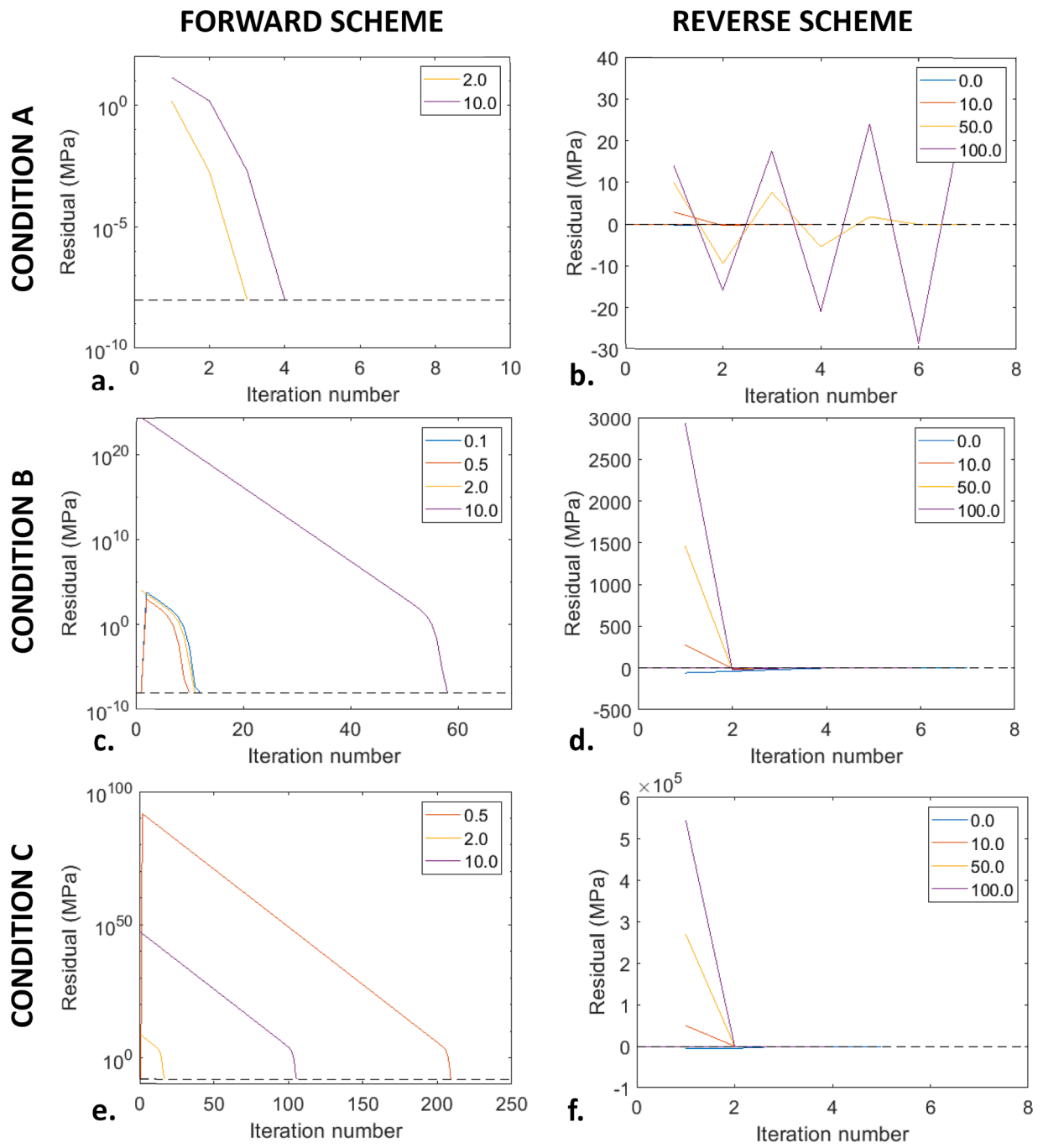

Fig. 4. Simulation results for a single 0.1 s increment with deformation rates defined by conditions A, B and C, showing the evolution of error residual as a function of N-R iterations for various initial guesses using the forward scheme (a, c & e) and the reverse scheme (b, d & f).

N-R iterations for each case and both schemes are shown in Fig. 4e and f. The lowest initial guess in the forward scheme ($\theta = 0.1$) resulted in an initial error of -5.54×10^3 MPa, the subsequent correction returned infinity and a solution wasn't found. The second lowest guess resulted in an initial error of -5.50×10^3 MPa and the subsequent error for the second iteration was 5.47×10^{91} MPa; this calculation then progressed in a stable manner and converged after 209 iterations. Overestimating the initial guess by a factor of two and ten resulted in initial errors of 3.61×10^8 MPa and 1.27×10^{47} MPa and the calculations required 17 and 106 iterations respectively. All calculations using the reverse scheme converged with five iterations or fewer and the error evolution towards the solution was stable. The initial error when guessing zero slip rate ($\theta = 0$) was significantly larger for this high strain rate condition -5550 MPa, however the solution was stable, and convergence was achieved in five iterations. Again, the error in the calculations using

initial guesses that were larger than the converged solution all went from positive to negative on the second iteration and all converged with four iterations.

These results demonstrate the behavior of each scheme when initiated with various initial guesses. In summary, the error in the forward scheme scales with the sinh() of the error, which can be very large or return infinity in extreme cases where stress is initially overestimated. For these cases (i.e., $\theta > 1$ here) and the calculation hasn't returned infinity, the solution progresses in a stable (monotonic) fashion to a converged solution. When stress is initially underestimated, the error is negative and stress correction for the following increment significantly overshoots; this can result in the return of infinite values on the second increment. In contrast, overestimating the slip rate when initiating the reverse scheme resulted in the largest initial errors and the calculation was unstable (nonmonotonic) for large initial guesses in the calculation for condition A. These comparisons confirm the behavior depicted in Fig. 2. Despite the larger values of θ used, the errors resulting from the various initial guesses were much lower for the reverse scheme compared to the forward scheme, and fewer iterations were required to reach convergence. This demonstrates the higher stability offered by the reverse scheme with the $\sinh^{-1}()$ function.

4.2. Multi-increment demonstration for a single slip system in one dimension

Of the calculations presented in the previous section, the initial guesses in all but the $\theta = 0.0$ case required prior knowledge of the solution which is not representative of solving CPFEM problems in practice. For conventional CPFEM simulations, the N-R loop must be initiated with a guess that is calculated using information about the incremental deformation and/or the solution values from previous increments. Using an initial guess of zero slip rate ($\dot{\gamma}_p = 0.0\ s^{-1}$) in the reverse scheme is not based on information from previous increments and offers a stable calculation which progresses to the converged solution as described in preceding sections. Therefore, all calculations using the reverse scheme presented in the remaining sections of this paper are initiated with zero slip rate,

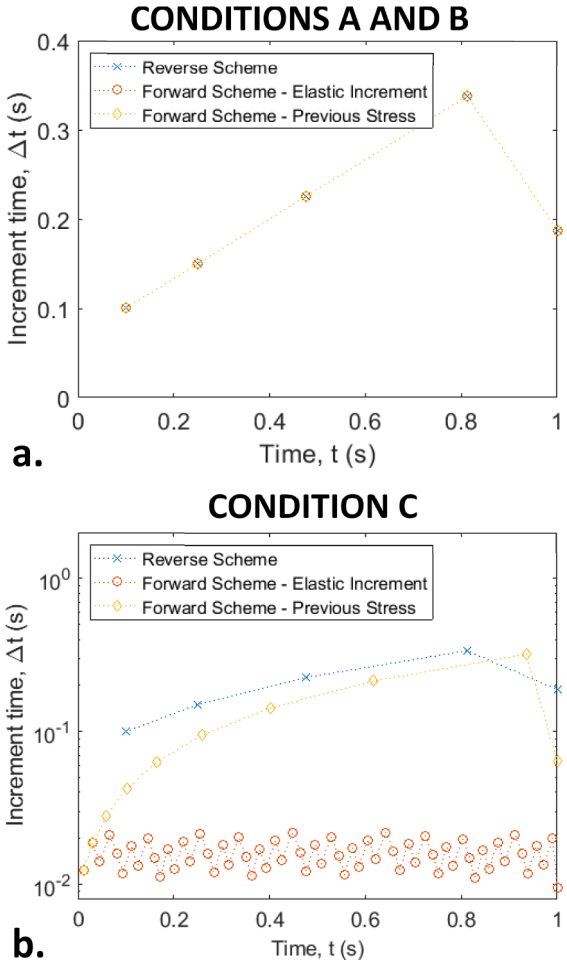

Fig. 5. Evolution in time increment resulting in converged solutions for (a) conditions A and B and (b) condition C in one dimension. Calculations used the reverse scheme and forward scheme initiated with initial guesses for stress based on an elastic increment and stress from the previous increment.

$\dot{\gamma}_p = 0.0\ s^{-1}$. Calculation of an initial guess for the forward scheme is more challenging due to the presence of a finite interval of stress which results in a successful calculation. Previous studies have used simple calculations based on the assumption that all strain in the increment is elastic (Eq. (32), providing an upper bound) (Dunne et al., 2007), or a perfectly plastic response where the guess in stress is simply taken from the previous converged increment (Eq. (33)), or more sophisticated approaches using analytical and numerical gradients of previous variables (Huang, 1991). For the purposes of comparison, the following two guesses for stress were used:

$$\tau_{(i=1)} = G\left(\gamma_{e(t)} + \Delta\gamma\right) = \tau_{(t)} + G\Delta\gamma \tag{32}$$

and,

$$\tau_{(i=1)} = \tau_{(t)} \tag{33}$$

where index $i = 1$ refers to the initial guess in the first iteration. The evolution of time increment was investigated for each of the schemes and guesses by using a simple algorithm based on increment convergence, where the increment time was increased by 50 % if the previous increment converged successfully and reduced by 50 % if the solution attempt failed. Solution failure was identified at the point variables were assigned infinity or NaN (i.e., 'Not a Number'). The total strain rates for conditions A, B and C were applied over a total time of 1 s and the initial time increment was set to 0.1 s. The calculation was therefore identical to that presented in the previous section for the first increment and first attempt (when $\Delta t = 0.1\ \ s$).

Results for evolution of increment time (Δt) for conditions A and B were identical for both schemes and all initial guess calculations studied; these results are shown in Fig. 5a. The calculations for each increment solved successfully resulting in a progressive increase in the Δt until the final increment, which was smaller to finish the solution at the total time of 1 s. For condition A, the penultimate increment (which had the largest time increment) for both stress guesses using the forward scheme required four iterations to converge, whereas the same increment for the reverse scheme required six iterations. For condition B, the number of iterations required to solve the penultimate increment using the forward scheme was 45 for the elastic increment guess and three for the previous stress guess; this demonstrates the higher accuracy of the guess based on the previous stress for a perfectly plastic material and constant strain rate condition. The number of iterations required to solve the penultimate time increment using the reverse scheme was six.

Results for condition C are shown in Fig. 5b. The calculation using the forward scheme initiated with the elastic increment guess required very small time increments with a maximum of 0.022 s, which required 249 iterations to solve. As described above, the previous stress guess is zero for the first increment which is an underestimation, thus a first time increment of 0.0125 s and 134 iterations was required for convergence. The higher accuracy of the previous stress guess for this constant strain rate and perfectly plastic material then enabled ever increasing time increments and the largest time increment in this calculation required only two iterations. Finally, all attempts to solve increments for condition C were successful with the reverse scheme and the time increment progressively increased with each increment as a result. The largest time increment was 0.3375 s and five iterations were required for convergence.

Results for the largest time increment in all calculations are summarized in Table 2.

4.3. Multi-increment demonstration for multiple slip systems in three dimensions

Comparing the performance of forward and reverse implicit schemes to calculate problems that include multiple slip systems in three dimensions is essential, since this is representative of typical crystal plasticity simulations conducted using the finite element method. The calculations were initiated for both schemes using the same initial guesses as for the 1D calculations. For the forward scheme in three dimensions, the guess based on an 'elastic increment' was calculated by:

Table 2
Maximum time increment (in parentheses) and corresponding number of iterations required for convergence, for both loading types and deformation rate conditions A, B and C, for each calculation method applied to a single slip system in one dimension.

No. of iterations for increment (max Δt, s)			
	Condition A	Condition B	Condition C
Reverse Scheme	6 (0.3375)	6 (0.3375)	5 (0.3375)
Forward Scheme - Elastic Increment	4 (0.3375)	45 (0.3375)	249 (0.022)
Forward Scheme - Previous Stress	4 (0.3375)	3 (0.3375)	2 (0.3204)

Table 3
Maximum time increment (in parentheses) and corresponding number of iterations required for convergence, for both loading types and deformation rate conditions A, B and C and for each calculation method.

No. of iterations for increment (max Δt, s)			
Uni-axial Loading	Condition A	Condition B	Condition C
Reverse Scheme	49 (0.3375)	33 (0.3375)	38 (0.3375)
Forward Scheme - Elastic Increment	6 (0.3375)	109 (0.3375)	375 (0.0134)
Forward Scheme - Previous Stress	5 (0.3375)	3 (0.3375)	1 (0.3204)
Shear Loading	Condition A	Condition B	Condition C
Reverse Scheme	88 (0.3375)	578 (0.3375)	7384 (0.3375)
Forward Scheme - Elastic Increment	4 (0.3375)	44 (0.3375)	55 (0.0044)
Forward Scheme - Previous Stress	4 (0.3375)	4 (0.3375)	4 (0.2703)

$$\boldsymbol{\sigma}_{(i=1)} = \mathbb{C} : \left(\boldsymbol{\varepsilon}_{e(t)} + \Delta\boldsymbol{\varepsilon}\right) = \boldsymbol{\sigma}_{(t)} + \mathbb{C} : \Delta\boldsymbol{\varepsilon}_{(t+\Delta t)} \tag{34}$$

and that based on the previous stress:

$$\boldsymbol{\sigma}_{(i=1)} = \boldsymbol{\sigma}_{(t)} \tag{35}$$

For the reverse scheme, the same zero slip rate ($\dot{\gamma}_{\mathrm{p}} = 0.0\ \mathrm{s}^{-1}$) on all slip systems was used as an initial guess.

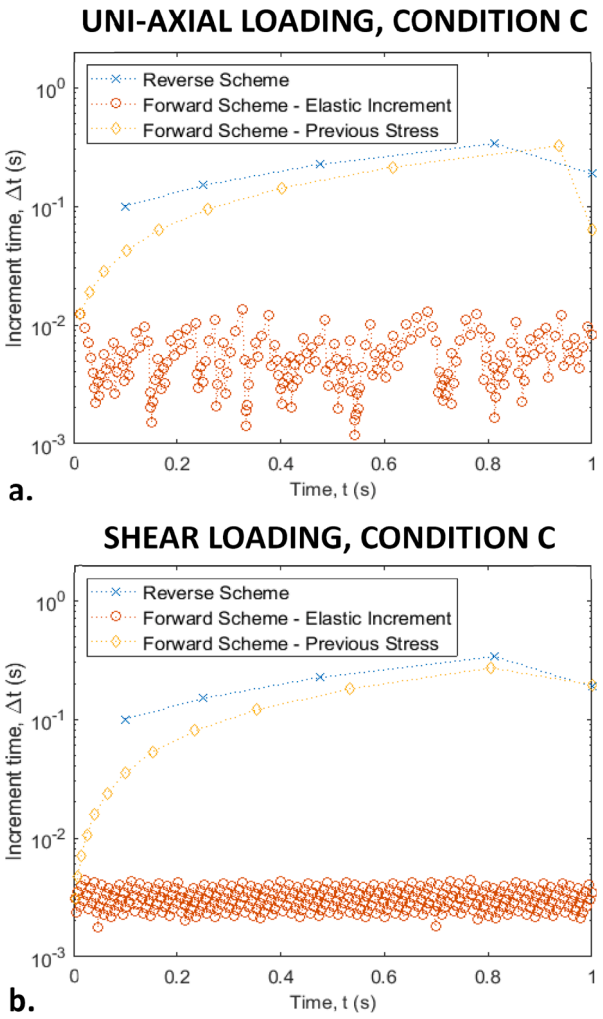

Fig. 6. Evolution in time increment resulting in converged solutions for (a) uniaxial and (b) shear loading and condition C in 3-dimensions. Calculations used the reverse scheme and forward schemes initiated with initial guesses for stress based on an elastic increment and stress from the previous increment.

The conditions of applied deformation rate in the form of velocity gradients for uniaxial loading and shear loading (iv, v and vi) as described in Section 3 were used for comparing the calculations in three dimensions. The largest time increment and corresponding number of iterations required to solve these calculations, are given for both uniaxial and shear loading types in Table 3.

For both loading types, the evolution in time increments for the three calculation methods were identical to the one-dimensional calculation for conditions A and B, with the time increments progressively increasing throughout the simulation time to a maximum of $\Delta t = 0.3375$ s. Unlike the forward scheme calculations, the time increments also progressively increased for calculations using the reverse scheme for condition C, which is also identical to that observed for the 1D calculations. Evolution of the time increment for both loading types under condition C is shown in Fig. 6 for the three calculation methods. For calculations using the forward scheme, the number of iterations per increment increased with increasing deformation rate (condition A to C) and the associated difficulty in solving increments ultimately led to a limitation in the size of the time increment for condition C. These results confirm the effect of the poor initial guess using the elastic increment calculation, which becomes worse with higher deformation rates. In contrast the previous stress guess is very accurate for this elastic-perfectly plastic material and only a small number of iterations are required to solve the largest increment when the material response is in a steady state. Far more iterations were required to solve the first increment when calculating with the previous stress guess, which limited the first time increment to 0.0125 s for the uni-axial loading and 0.0031 s for the shear loading, these required 292 and 30 iterations respectively.

The shear stress and plastic shear strain on each slip system was the same for all calculation methods and is shown for the two loading types subject to deformation rate condition C in Fig. 7. For the uni-axial loading type, the eight slip systems ($k = 1,\ 3,\ 4,\ 6,\ 7,\ 9,\ 10,\ 12$ as defined in Appendix A) have the same shear stress and equal shear strain, which tends towards the applied value of $\dot{\gamma} = 1.36\ s^{-1}$ at 1 s, due to the viscous response of the material. Slip systems have a distribution of shear stress under the applied shear loading. Again, shear strain rate approaches the applied value for condition C, however the shear stress on all other slip systems is greater than the critical value ($\tau_c^k = 1$ MPa), which results in relatively low levels of slip rate and strain accumulation on these systems also. It can be seen in Table 3 that convergence in calculations using the reverse scheme was relatively fast for the uni-axial loading, but far more iterations were required for the shear loading case. This agrees well with the findings by McGinty (2001), who observed that convergence is dominated by error reduction on the systems with negligible slip rates. In contrast, calculations using the forward scheme with an initial guess based on an elastic increment were seemingly unaffected by the distribution of stress and slip rate on

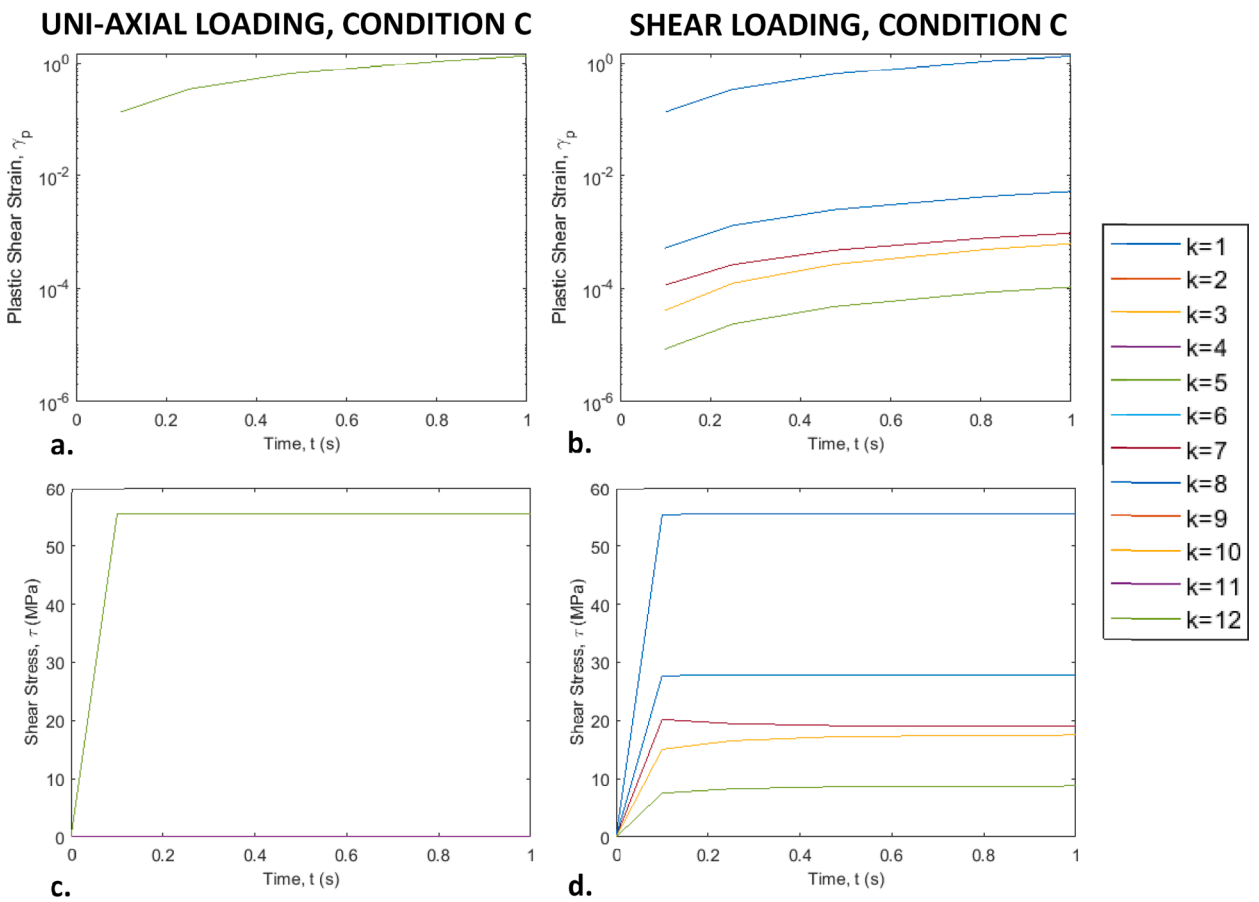

Fig. 7. Plastic shear strain (slip) and shear stress for all slip systems subject to uni-axial (a & c) and shear (b & d) loading types and deformation rate condition C.

multiple systems.

The same calculations for shear loading and condition C were conducted again with $\tau_c^1 = 1.0$ MPa and $\tau_c^{2-12} = 1.0 \times 10^6$ MPa, which essentially removed all the negligible systems, keeping just slip system $k = 1$ in the calculation. Additionally, the step size (ϕ) for the corrector used in the reverse scheme (see Eq. (27)) was set to 1.0. Compared to the calculation that included all slip systems, the evolution in time increment was identical for the reverse scheme and forward scheme initiated with a guess based on the previous stress and the number of iterations required to solve the penultimate (largest) time increment was five for the reverse scheme and one for the scheme using the guess based on the previous stress. The maximum time increment for the scheme with initial guess based on an elastic increment was 0.0032 s and required 40 iterations to solve. The results for the reverse scheme and forward scheme using the previous stress guess are nearly identical to the one-dimensional calculation using the reverse scheme and demonstrate that the additional iteration required to solve similar conditions of stress and strain using the reverse scheme, is primarily caused by the addition of multiple slip systems.

The formulation presented in Section 2 introduced a new error function for the reverse scheme which is based on the resolved shear stresses on each slip system. The number of iterations required to solve 3-dimensional problems using this scheme and error function was significantly higher than the equivalent one-dimensional calculations. The lower convergence rate in the 3D problems may be due to the following two reasons:

i. In addition to solving the stress to achieve the correct balance of elastic and plastic strain (like the 1D calculation), this scheme must also find the correct values for the interdependent resolved shear stresses that satisfy equilibrium. It is likely that the addition of multiple degrees of freedom with these constraints is responsible for reducing the convergence rate in these calculations.
ii. The tangent of the error function given in Eq. (24) is approximated as a diagonal matrix by omitting off diagonal components that relate to the interdependency of slip systems, which likely results in less optimal evolution of shear strain rates towards convergence.

4.4. Convergence rate and hybrid scheme for optimal performance

The rate of convergence for the different schemes was investigated using data from the three-dimensional calculations with multiple slip systems for the shear loading type and condition C as described in the previous section. These are shown in Fig. 8 for the time increments which required the most iterations, alongside the corresponding evolution in shear stress and slip rate for each slip system. As shown in Eq. (10), the amount the error is reduced by is proportional to the error at each iteration, thus the natural logarithm of the error versus iteration number has clear linear segments. The rate of convergence within each linear segment can be found by fitting a line of the form:

$$\ln(r) = \ln(r_0) - Mi \tag{36}$$

where r_0 is the initial error, i is the iteration number and M is the convergence rate, as shown for the various linear segments in Fig. 8. The convergence rate for the forward scheme is approximately 1.0, then rapidly increases in the final few iterations, a result which is also reflected for the one-dimesional problems presented in Fig. 4. As shown in Fig. 8c, a significant overshoot appears to exist on the fourth iteration which is followed by relatively linear evolution of shear stress as a function of iteration. Due to the exponential form of the slip law Initial values for slip rate are relatively high in the calculations using the forward scheme, thus a logarithmic y-axis is used to present only the positive values in Fig. 8e. During iteration, the shear stress and slip rate on three slip systems change sign, which is evident by discontinuous plots of the slip rate.

The convergence rate in the reverse scheme has three different segments. Initially the error reduces rapidly with $M \approx 0.5$ and shear strain rates for multiple slip systems increase on each iteration, thereby reducing the large stresses associated with the zero-slip rate initial guess. Following this first segment, the convergence rate reduces dramatically which coincides with the subsequent reduction of shear strain rates on some slip systems, due to stress relaxation caused by slip on the highest stressed systems. The shear strain rates on the lower stressed slip systems reduce to relatively small values or simply return to zero if the resolved shear stress reduces below the critical value for that slip system. Given the large strain rate and resultant high proportion of flow stress due to viscoplasticity in this condition, all resolved shear stresses are above the relatively low critical resolved shear stress of 1 MPa for each slip system and small amounts of slip exist on all 12 slip systems as shown in Fig. 7d. Once the shear strain rate for the most active slip system ($k = 1$) is approximately converged, the convergence rate increases to solve the relatively small shear strain rates on the other slip systems.

The activation of all 12 slip systems is a result of the high deformation rate imposed by condition C and material parameters used in this study; this is responsible for the relatively low convergence rate in the reverse scheme and highlights a significant property of the reverse scheme. The convergence rate is initially rapid and reduces the error to <100 MPa after just 14 iterations in Fig. 8b, this early stage of the solution provides a sufficient approximation to be used as an initial guess in the forward scheme with a higher convergence

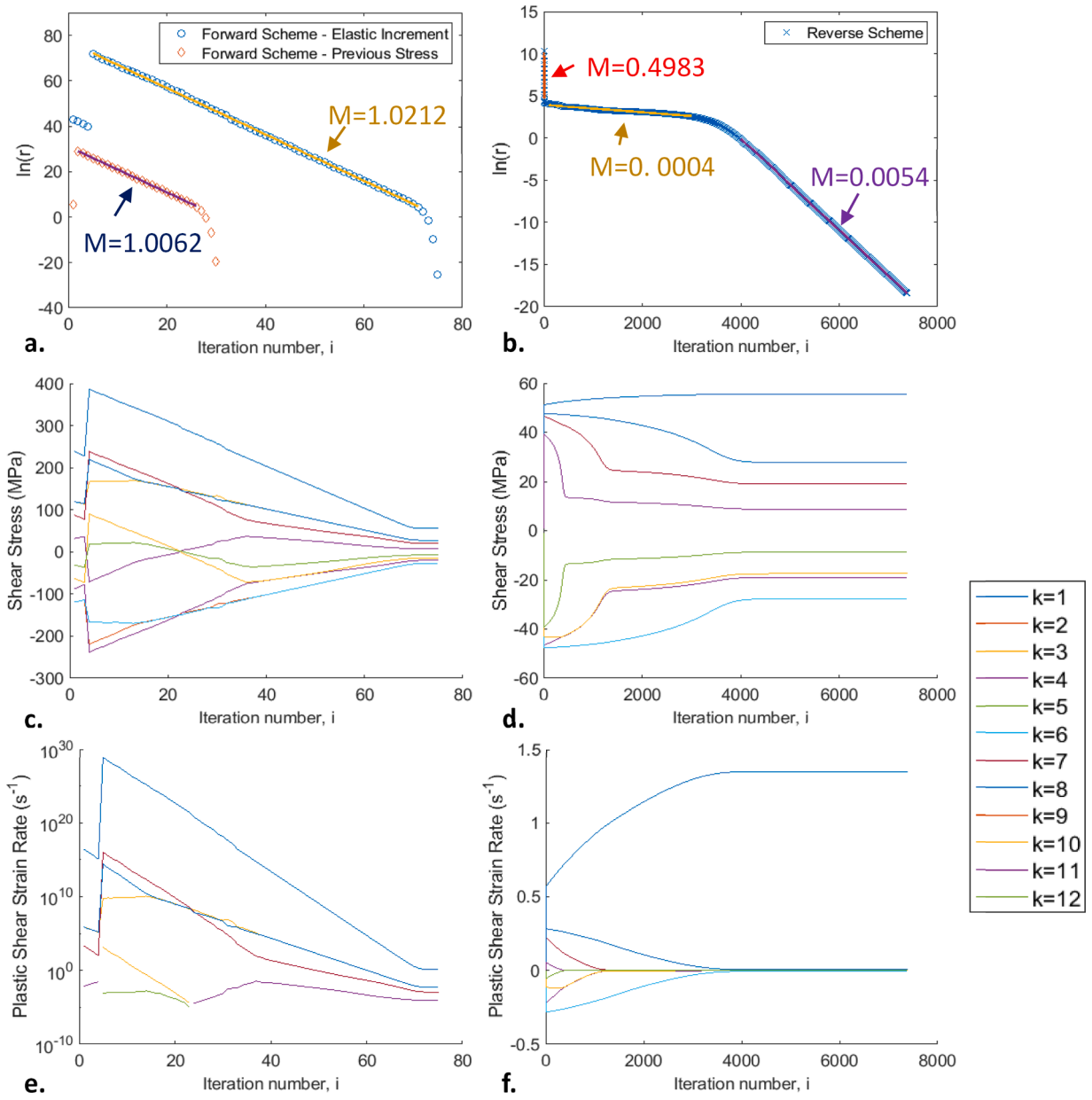

Fig. 8. Convergence rate for the largest time increments in the calculations for condition C solved in three dimensions using (a) the forward scheme and (b) the reverse scheme, with corresponding evolution of the shear stresses and shear strain rates on each slip system for the forward scheme using an elastic increment guess (c & e) and the reverse scheme (d & f).

rate.

We now introduce a hybrid scheme, that first uses the reverse scheme to calculate an approximate solution for stress, which is then used as an initial guess in the forward scheme. The reverse scheme is used for the error range where the convergence rate is at its highest (i.e., in the region where $M \approx 0.5$), and the solution is likely outside of the interval of convergence for the forward scheme. A useful feature of the reverse scheme initiated with a zero slip rate guess is shown in Fig. 8d, where the shear stresses are initially high and subsequently reduce towards a converged solution. The stress is overestimated after the first few tens of iterations, which supports the successful transition to the forward scheme because it is initiated with an overestimate guess. This facilitates a stable solution, reducing the stress towards convergence and without the risk of overshoot that is associated with stress underestimation, as depicted in Fig. 2a and demonstrated in Section 4.1.

The Jacobian determinant, J_f, for the forward scheme (i.e., the determinant of the matrix given by Eq. (12) provides a measure of the behavior and stability of the forward scheme and could be used as a metric controlling transition from the reverse to the forward scheme. The Jacobian determinant is directly representative of the numerical problem and is a function of the slip law parameters and

thus provides a metric that is relatively general to all material parameters. The derivative of the slip law with respect to the resolved shear stress, $\frac{d\dot{\gamma}_p^k}{d\tau^k}$, given in Eq. (15), is the primary component of the Jacobian and its maximum has a close trend with the Jacobian determinant as a function of iteration. Given the relatively large computational expense of computing the determinant of a 6×6 matrix, for numerical efficiency the maximum value of the slip law derivatives integrated over the time increment was investigated as a transition metric:

$$\lambda = \max\left(\frac{d\gamma^k}{d\tau^k}\right) = \max\left(\alpha\beta\cosh\left[\beta\left(\left|\tau^k\right| - \tau_c^k\right)\right]\Delta t\right) \tag{37}$$

Components of this derivative start with large values for the first few iterations in the reverse scheme initiated with a zero slip rate guess and they can even be assigned 'NaN' or 'Inf', i.e., a floating-point overflow error is returned. After this, the values reduce rapidly with each iteration, with starting values up to the maximum for an 8-byte, double precision variable ($\sim 1 \times 10^{308}$). The number of iterations required to solve both loading types under the deformation rate of condition C was investigated for various transition thresholds, ζ, based on the condition when $\lambda < \zeta$. These calculations were conducted over a period of 1 s and with a fixed time increment of $\Delta t = 0.1$ s. The number of iterations required to solve the last increment for each calculation is shown in Fig. 9.

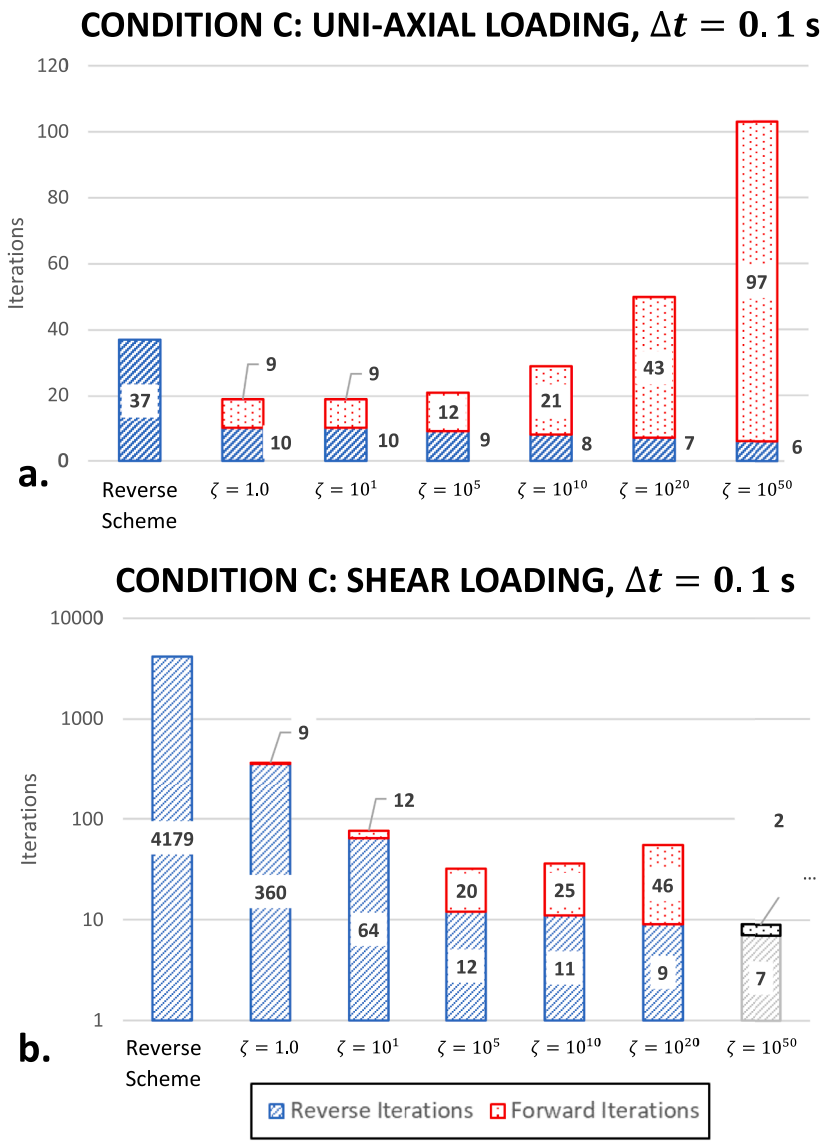

Fig. 9. Number of iterations required to solve the final increment for calculations using the hybrid scheme with different transition thresholds, ζ. The calculations were for the 3D, multiple slip system case subject to the condition C deformation rate and for the (a) uni-axial loading and (b) shear loading types. The calculation was over a time of 1 s with fixed time increments of $\Delta t = 0.1$ s.

All but one of the calculations presented in Fig. 9 resulted in a converged solution. The threshold $\zeta = 10^{50}$ MPa^{-1} was too high for the shear loading case, where only seven iterations were required to meet this criterion in the reverse scheme and the forward scheme was initiated with a solution that resulted in divergence and solution failure. Compared to the reverse scheme alone, the hybrid scheme required significantly fewer total iterations to reach a converged solution. As the threshold ζ increased, the number of iterations required by the reverse scheme decreased and the corresponding number of iterations required by the forward scheme increased. The total number of iterations was smallest when the number of iterations required by each scheme was approximately equal, which for the calculations studied corresponds to a threshold in the range $\zeta = 10^{1}$ to 10^{5} MPa^{-1}.

Given that λ (in Eq. (37)) is the primary component of the Jacobian in the forward scheme and it includes the slip law parameters for the material being modeled, it is argued above that a threshold based on this value should be general to all materials. The selection of the threshold value, ζ, should be based on optimal convergence rate for computational efficiency and ensuring solver robustness, to ultimately avoid cutbacks in the time increment. The computation cost of iteration in each scheme is likely different, however optimal efficiency is likely found for a threshold where the total number of iterations is minimized. Referring to solver robustness, the hybrid scheme can fail either because the transition threshold is selected to be too high that the solution passed to the forward scheme is outside the interval of convergence (i.e., as shown in Fig. 9 for shear loading and $\zeta = 10^{50}$ MPa^{-1}), or the threshold is selected lower than the converged value. The value of λ for the converged solution was 0.0272 and 0.027 MPa^{-1} for the uni-axial and shear loading types respectively, which is well below the threshold values studied here. However, for lower rate dependent materials that have more extreme non-linearity in slip rate, the interval of convergence becomes smaller, and these constraints may become important.

5. Implementation into a CPFEM framework

The hybrid scheme was implemented in a user material subroutine (UMAT) for solving finite element simulation with Abaqus/CAE 2020® software with all default settings, apart from increasing the default maximum number of solution attempts from five to 60, which avoided simulation aborts due to this limit in all cases. The original UMAT was based on that described by Dunne et al. (2007) and the reverse scheme was incorporated as an additional subroutine and called just prior to the pre-existing N-R solver based on stress. This CP formulation updates state variables including rotations explicitly at the end of each increment, thus full kinematics of large deformations were accounted for. In this section results from two models are presented. Firstly, simulation of a single crystal plate with a hole under tensile loading was conducted to investigate the performance of the hybrid scheme. A final demonstration is presented for a more challenging simulation, which comprises of a polycrystalline Zircaloy-4 plate, subject to cyclic shear loading, which includes material hardening and crack propagation.

5.1. Simulation of a single crystal plate with a hole

The results presented in Section 4 are limited to pointwise calculations for uni-axial tension and one type of shear loading. Prior to yielding, a plate with a hole under tension provides a wide range of stress states from uniaxial tension on the horizontal axis, transitioning to pure shear at 45° from the horizontal axis and compression on the vertical axis, whose magnitude drops off from peak values adjacent to the hole outwards from the hole centre. To demonstrate the performance of the different solver methods for a broad range of stress states and different crystal structures, CPFEM simulations of the single crystal plate with a hole were performed for two

Table 4
Material properties and slip rate parameters for Zircaloy-4 (Liu et al., 2022).

Property	Symbol (s)	Value	Unit
Young's Modulus	E_{11}	98.308	GPa
	E_{22}	132.208	GPa
Shear Modulus	G_{12}	32.010	GPa
Poisson's Ratio	ν_{12}	0.4006	
	ν_{13}	0.2375	
Burgers vector	b	3.2×10^{-4}	μm
Slip rate parameter <a> slip systems	α^{1-12}	3.217×10^{-4}	s^{-1}
Slip rate parameter <a+c> slip systems	α^{13-30}	8.16×10^{-4}	s^{-1}
Slip rate parameter <a> slip systems	β^{1-12}	0.1695	MPa^{-1}
Slip rate parameter <a+c> slip systems	β^{13-30}	0.4301	MPa^{-1}
Basal <a> (k = 1 to 3)	τ_c^{ba}	204.0	MPa
Prismatic <a> (k = 4 to 6)	τ_c^{pr}	153.0	MPa
Pyramidal <a> (k = 7 to 12)	τ_c^{py}	153.0	MPa
pyramidal <a+c> 1st (k = 13 to 24)	τ_c^{py1}	532.4	MPa
pyramidal <a+c> 2nd (k = 25 to 30)	τ_c^{py2}	2662.1	MPa

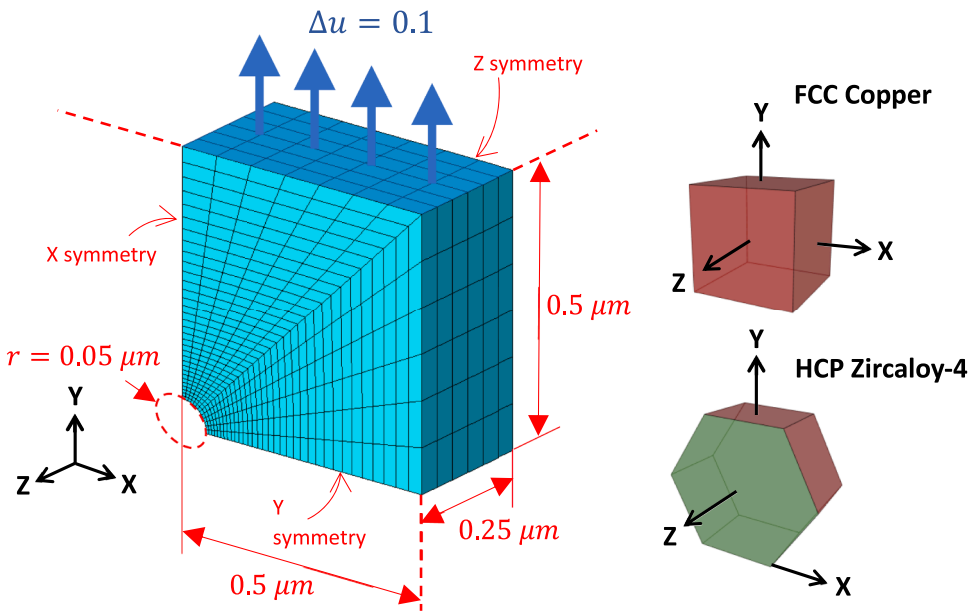

Fig. 10. Finite element model of a plate with a hole, utilising symmetry in the X, Y and Z planes, and crystal orientations for the FCC and HCP materials indicated.

materials. These were FCC copper with 12 slip systems and identical properties to those described above and Zircaloy-4, with 30 slip systems and properties given in Table 4 (Liu et al., 2022). All simulations for both materials were conducted with no hardening, thus these properties remained constant. For the FCC copper material $\chi = 2.0$ was maintained for the calculation of step size in Eq. (28), however for the FE simulations with the HCP Zircaloy-4 material $\chi = 1.25$ was required to ensure solution stability.

The model of the plate with a hole is shown in Fig. 10, with the crystal orientations indicated for the FCC and HCP materials. The plate dimensions were 1 × 1 μm, with a thickness of 0.5 μm and a hole radius of 0.05 μm, which was modeled using symmetry conditions in all three axes. The mesh included 2574 quadratic hexahedral elements with reduced integration (C3D20R). Displacement loading of 0.1 μm was applied to the top surface over a duration of 0.5 s, with an initial and maximum time increment set to 0.5 s.

Results for the performance of each simulation is shown in Fig. 11. Here we differentiate failed solution attempts between those that failed due to convergence failure within the CP solver, hereafter referred to as a 'CP cutback' in the time increment, and those that failed due to a problem with the global finite element simulation within the Abaqus standard solver, referred to as 'FE cutback'. FE cutbacks occurred due to 'excessive element distortion', the 'rate of convergence is slow' and that the 'solution appears to be diverging'.

Overall, the hybrid scheme with a transition tolerance of $\zeta = 10^{10}$ MPa^{-1} had superior performance compared to the forward scheme with stress based on an elastic increment. The transition tolerance of $\zeta = 10^{20}$ MPa^{-1} was clearly insufficient and even resulted in a slight increase in the number of CP cutbacks compared to the forward scheme. The number of CP cutbacks reduced as the transition tolerance decreased and for $\zeta = 10^{2}$ MPa^{-1} and lower there were zero CP cutbacks in the simulations of copper. This result is remarkable considering that the initial time increment was set to the total simulation time of 0.5 s, because the CP solver converged in this extreme case and the attempt only failed due to excessive element distortion. The simulation performance of these cases was entirely limited by the finite element solver within Abaqus. For simulations on the Zircaloy-4, the initial time increment of 0.5 s was too high and the first six attempts of the first increment failed due to convergence failure of the CP solver for all schemes. Following this, the CP solver never failed for all attempts using the hybrid scheme with a transition tolerance of $\zeta = 1.0$ MPa^{-1} and the simulation was entirely limited by the Abaqus finite element solver.

The results for the forward scheme with an initial guess based on previous stress reflect the earlier observations for these elastic-perfectly plastic materials, where the solver performance performed well after yield. All CP cutbacks that occurred in the simulation of

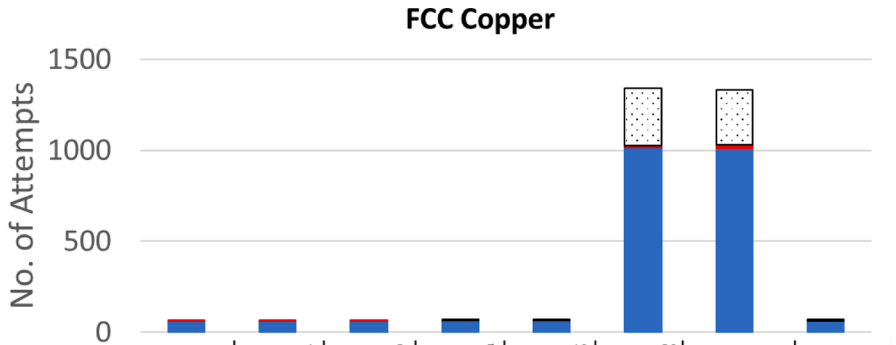

a.

	$\zeta = 1.0$	$\zeta = 10^1$	$\zeta = 10^2$	$\zeta = 10^5$	$\zeta = 10^{10}$	$\zeta = 10^{20}$	Forward Scheme - Elastic Increment	Forward Scheme - Previous Stress
Attempts	67	67	67	66	66	1343	1332	71
Successful Increments	61	61	61	60	60	1016	1013	61
FE Cutbacks	6	6	6	5	5	9	17	2
CP Cutbacks	0	0	0	1	1	318	302	8
Max Δt (s)	0.0116	0.0116	0.0116	0.0119	0.0119	0.0020	0.0008	0.0116

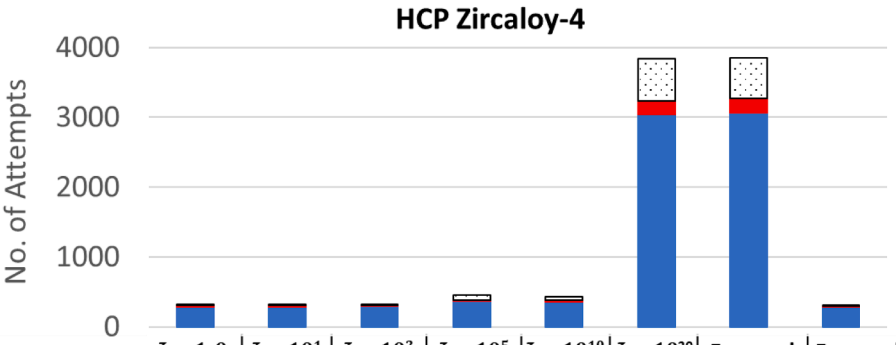

b.

	$\zeta = 1.0$	$\zeta = 10^1$	$\zeta = 10^2$	$\zeta = 10^5$	$\zeta = 10^{10}$	$\zeta = 10^{20}$	Forward Scheme - Elastic Increment	Forward Scheme - Previous Stress
Attempts	312	311	318	448	430	3837	3855	311
Successful Increments	289	288	293	372	362	3040	3065	288
FE Cutbacks	17	15	16	15	16	192	207	12
CP Cutbacks	6	8	9	61	52	605	583	11
Max Δt (s)	0.0038	0.0038	0.0038	0.0035	0.0036	0.0006	0.0006	0.0035

Fig. 11. Simulation performance for (a) FCC copper and (b) HCP Zircaloy-4 material properties. Number of solution attempts, successful increments, and failed increments, due to simulation failure globally (FE cutback) or failure of the crystal plasticity solver (CP cutback). The maximum time increment post yield ($t > 0.025$ s) also given in the table insert.

copper were the initial eight failed attempts for the first increment, whereas all but one of the CP cutbacks in the simulation of Zircaloy-4 were at yield (i.e., within the first three increments). For both materials, the total number of simulation attempts was over an order of magnitude lower for the hybrid scheme with a transition tolerance of $\zeta = 10^5$ MPa^{-1} and for the forward scheme with a guess based on the previous stress, compared to the latter with a guess based on an elastic increment.

5.2. *Demonstration on polycrystalline model with cyclic loading, hardening and crack propagation*

For rigorous performance evaluation of the hybrid scheme, it is applied to a highly non-linear engineering problem in this section. Specifically, an industrially relevant case of microstructural fatigue crack propagation in Zircaloy-4 is studied. Using electron backscatter diffraction (EBSD) data from polycrystalline Zircaloy-4 (Thomas et al., 2019), a CPFE model is constructed to represent a 50 × 50 μm region. A key addition and challenge for the current CPFE model is strain gradient, dislocation-based hardening under plastic deformation, the details for which are given below. As illustrated in Fig. 12, cyclic displacement (strain) controlled loading is applied

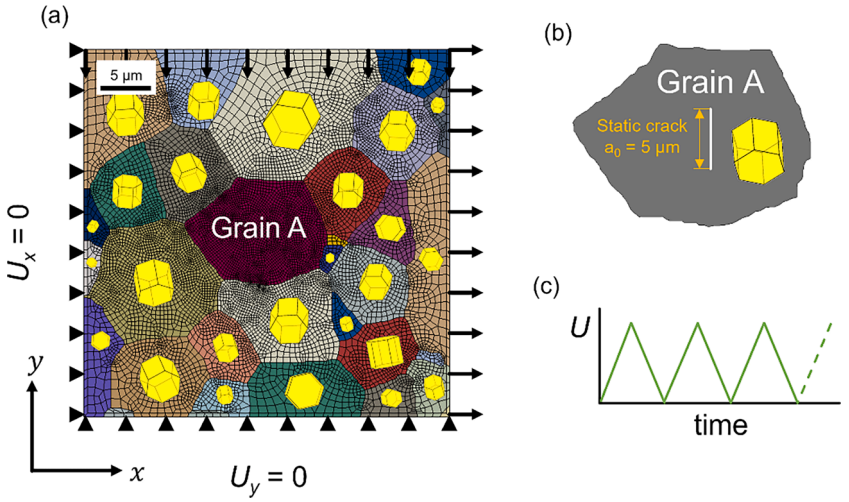

Fig. 12. Configuration of polycrystal fatigue crack growth model. (a) Boundary conditions and meshing of 50 × 50 μm polycrystal region of interest. Uniform displacement boundary conditions are applied to all outer edges of the model as shown, giving a peak total strain in the x-direction of 0.75 %. Tangential displacements are distributed linearly, as described in the text. (b) Initial location and morphology of crack within Grain A, measuring 5 μm in the y-direction. (c) Cyclic displacement boundary conditions; a peak strain is applied and is fully reversed within each cycle.

to the boundaries of the region, and an initial 5 μm crack is positioned within Grain A.

Fig. 12a shows that the displacement boundary conditions U_x and U_y, are applied in the x and y directions respectively, to all outer edges of the polycrystal model, which broadly reflect the boundary displacements measured using *in-situ* digital image correlation (DIC) of the same microstructure region under monotonic uniaxial loading (Thomas et al., 2019). A tensile strain is applied in the x-direction during the load up phase of the fatigue cycle (i.e., $dU_x/dt > 0$), while a compressive strain is applied in the y-direction. The proportion of tensile to compressive strain is estimated based on the DIC data (Thomas et al., 2019) at 3 % strain; this proportion is maintained in the current analysis up to a peak global strain of 0.75 % at $t = 37.5$ s. For the second half of the cycle this loading is reversed (i.e., $dU_x/dt < 0$). The total time for each cycle (with maximum applied global strain of 0.75 %) is 75 s, which gives a mean applied strain-rate of $\pm 2 \times 10^{-4}$ s^{-1}. These conditions are consistent with laboratory fatigue testing of zirconium alloys (Wisner et al., 1994). To prevent boundary-induced strain localization, tangential displacements are controlled at all outer edges, i.e., x- and y-displacements vary linearly along all edges in the x- and y-directions, respectively. Until now, all simulations described above have been based on an elastic-perfectly plastic material behavior, i.e., τ_c^k was constant. For the simulations described in this section non-linear hardening was implemented by the following simple Taylor hardening law (Wilson et al., 2018):

$$\tau_c^k = \tau_0^k + Gb\sqrt{\rho_{GND} + \rho_{SSD}} \tag{38}$$

where τ_0^k are the initial critical resolved shear stresses for each slip system k, G is the shear modulus (taken here as the basal plane shear modulus since slip activity in Zircaloy-4 is predominantly <a> type) and b is the Burgers vector as given in Table 4. Non-linear hardening due to the density of geometrically necessary dislocations (GNDs), ρ_{GND}, based on strain gradients, i.e., lattice curvature is incorporated here (Xu et al., 2021). Linear strain hardening based on the evolution of statistically stored dislocation (SSD) density, ρ_{SSD}, with increasing plastic strain is also accounted for. SSD density is given by $\rho_{SSD} = \gamma^{st} p$, where $\gamma^{st} = 130$ μm^{-2} (Hardie et al., 2022) is the hardening coefficient and p is cumulative effective plastic strain.

A 5 μm crack is placed within Grain A to initiate fatigue crack propagation, which is modeled using the eXtended Finite Element Method (XFEM) (Belytschko and Black, 1999). A stored energy density (SED) fracture criterion is used to control the rate of crack propagation, while the maximum slip criterion is used to control crack path (see Wilson et al. (2018) for the mechanistic basis for this methodology). A low value for critical SED of 1.5 Jm^{-2} (value at which the crack will extend) is selected in the current analysis to permit crack growth within a reasonable number of simulated fatigue cycles. The results of this analysis using (i) the hybrid scheme with a transition tolerance of $\zeta = 1.0$ MPa^{-1}, and the forward schemes with initial guess based on (ii) an elastic increment, and (iii) the previous stress are presented in Fig. 13.

Fig. 13a shows the evolution of simulation step time with number of increments during the first fatigue cycle using each solver method. For illustration, both the number of successful increments and total number of increment attempts (successful or otherwise) are included, demonstrating that for all cases, approximately 35–37 % of increments are unsuccessful; the highest proportion of unsuccessful increments is in the forward scheme with stress guess based on an elastic increment. Overall, both the hybrid scheme and the forward scheme based on previous stress offer significant improvements over the forward scheme based on elastic increment in terms of number of increments, which is homologous to CPU simulation time. For each case, there is a distinct transition in the increment-time trend, particularly for both forward scheme methods; this highlights the effect of the elastic-plastic transition on solver performance. Towards the end of the loading phase of the first cycle, the step time-increment gradient for the forward scheme based on

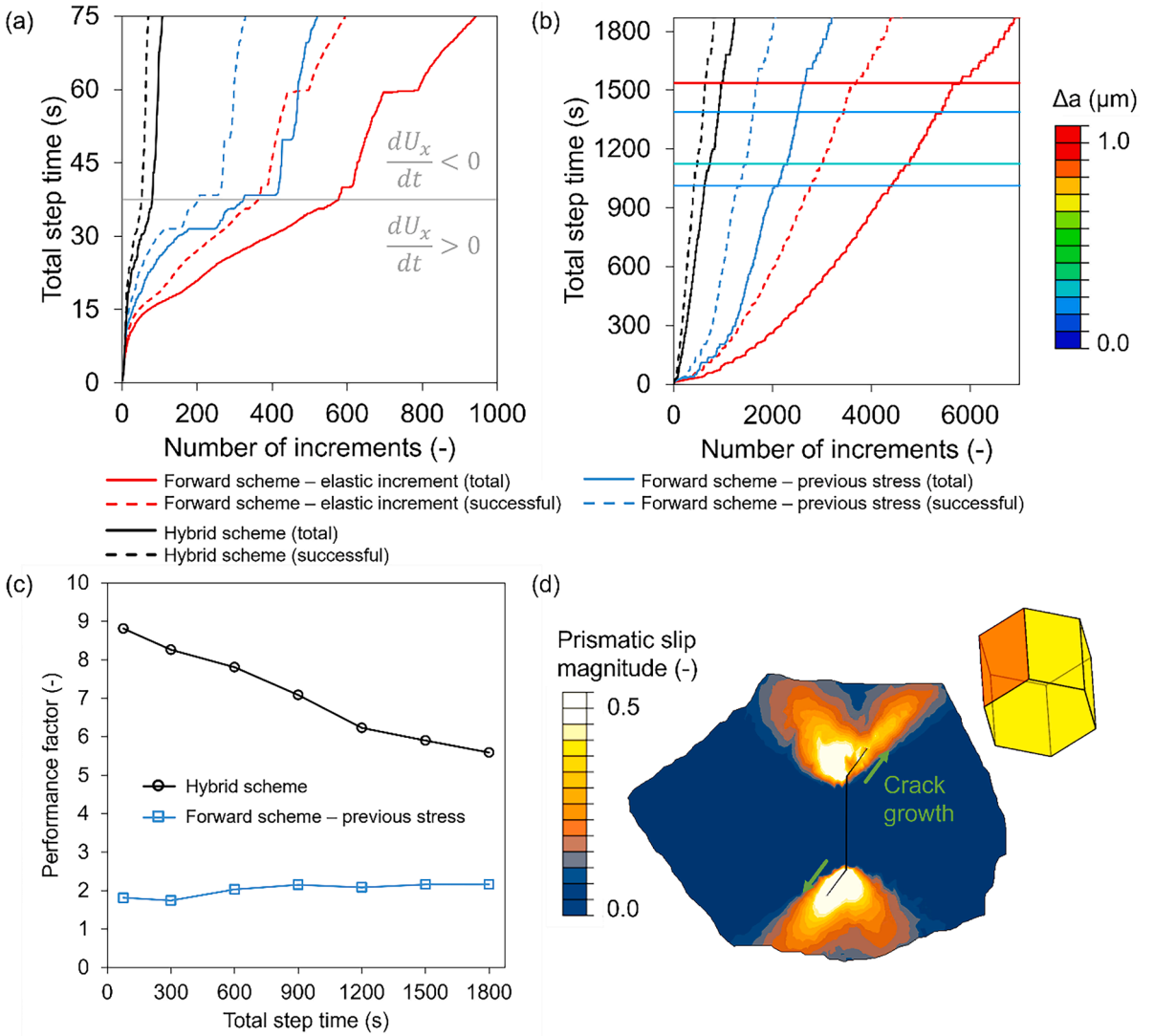

Fig. 13. Comparison of solver performance in short fatigue crack propagation study. (a) Relationship between the total number of increments and total step time for a single fatigue cycle (duration of 75 s). Comparison is made between the hybrid scheme and forward scheme initiated with guesses based on elastic increment and previous stress, in terms of the number of successful increments and the total number of increment attempts, successful or otherwise. The horizontal grey line represents the time at which the direction of applied displacement is reversed. (b) The same comparison as made in (a) for 25 fatigue cycles. Points at which crack propagation occur are represented via horizontal lines, the colors of which represent the magnitude of crack extension, Δa. (c) Ratio between the total number of increments using the forward scheme with guess based on elastic increment and (i) hybrid scheme and (ii) forward scheme based on previous stress, respectively, at various step times. (d) Crack path and corresponding prismatic slip field (for most active slip system) after 25 fatigue cycles.

Table 5
Summary of solver method performance after approximately 25 fatigue cycles (step time = 1800 s).

	Forward scheme	Previous stress	Hybrid scheme
Total increment attempts	6578	3015	1174
Successful increments	4188	1937	780
FE cutbacks	18	8	28
CP cutbacks	2372	1070	366

previous stress is shown to decrease, indicating poorer performance at higher levels of plastic strain. This is likely due to the increased rate of hardening, which is unaccounted for in the initial stress guess using this method. The gradient using the hybrid scheme, however, is shown to change marginally throughout the cycle, demonstrating overall best performance. An interesting characteristic of

both forward schemes is that at different step times, there are plateaus in the respective trends, indicative of very small increments due to extreme non-linearity. This is juxtaposed by the hybrid scheme result, which demonstrates its robustness. Fig. 13b presents the same data as in Fig. 13a for approximately 25 fatigue cycles, during which there are several occurrences of crack propagation. For multiple cycles, the relative performance of the hybrid scheme and the forward scheme based on elastic increment remain comparable to that in the first cycle, while a more significant difference is apparent using the conventional forward scheme based on previous stress increment. The latter shows the greatest increase in step time-increment gradient, i.e., improved performance with increasing cycle number. This is attributed to the progressive saturation of material response under fatigue; as the material hardens, cyclic plasticity is reduced and hence, the performance of forward schemes is improved. However, upon crack propagation, as indicated by horizontal lines in Fig. 13b, the forward scheme with guess based on elastic increment is least stable particularly for larger crack propagation increments (see color-bar). After the last crack propagation event (step time $\approx$ 1500 s), there is a dramatic reduction in step time-increment gradient using the forward scheme based on elastic increment, while the hybrid scheme and forward scheme based on previous stress remain less affected. As the crack propagates, the high stress concentration around the crack tip enters a region of low plasticity, and therefore, subsequent cycles manifest large plastic strain increments (until a more stable state is reached); this re-introduces extreme slip conditions that are challenging for the CP solver. An overall summary of solver performance (at step time $=$ 1800 s) is presented in Table 5, which highlights the vast improvement offered by the hybrid solver. Interestingly, the number of FE cutbacks (due to FE force equilibrium) is increased when using the hybrid solver; this is likely due to an increase in equilibrium convergence issues resulting from increased step time increments.

The total number of increments, successful or otherwise serves as an appropriate proxy for CPU simulation time in this study. Hence, a performance factor was defined as the ratio of total attempts between the hybrid scheme or the forward scheme with guess based on previous stress to the conventional forward scheme that uses an initial guess based on an elastic increment. Fig. 13c shows the evolution of this quantity with simulation step time for both the hybrid scheme and forward scheme based on previous stress. As anticipated, the hybrid scheme demonstrates the greatest improvement with performance factors in the range from six to nine, while those using the forward scheme based on previous stress large remain at two for the entire simulation. Cyclic hardening in this simulation reduces plasticity and led to less extreme conditions of plasticity for the solver, thus relative differences in solver performance are most evident within the fatigue first cycle.

6. Discussion and conclusions

The inverted slip law implemented in the reverse scheme, which calculates shear stress as a function of shear strain rate, offers two key advantages. Firstly, the NR loop in the reverse scheme can be initiated with zero slip rate on all slip systems ($\dot{\gamma}_{\mathrm{p}}^{k} = 0\ \mathrm{s}^{-1}$), which guarantees starting the solver within the interval of convergence for this system of equations. This initial guess requires no knowledge of previous state variables or boundary conditions and provides a stable starting point, free from large or infinite numbers that commonly limit the performance of conventional (forward) schemes using exponential based slip laws. Secondly, accounting for the continually decreasing gradient of the reverse form of the slip law, the shear strain rates on each slip system can be increased with each iteration in a stable manner and without overshoot. Whilst these advantages were demonstrated in this study, the reverse scheme suffered from relatively poor convergence rate for calculations where multiple slip systems are activated. It has been recognized that solvers based on the inverted slip law spend much of the solution time satisfying convergence for lower stressed slip systems with negligible slip rate (McGinty, 2001). The low convergence rate of the reverse scheme here was also due to the diagonalized slip system stiffness matrix, $\widetilde{\mathbb{G}}$, within the Jacobian, which treated slip systems independently in the corrector definition. Whilst this approximation was essential to provide an invertible Jacobian with full rank, the resultant inaccuracies became apparent for conditions where multiple slip systems were active, and a small step size was required within the corrector to ensure stability. In contrast to the HCP zircaloy-4 material model, the FCC copper material with 12 identical slip systems provides more solver stability and a larger step size was feasible. Deactivating all but one slip system by increasing their respective critical resolved shear stresses, confirmed that the lower efficiency was the result of having multiple active slip systems and not the 3-dimensional nature of the calculation. Despite the lower efficiency of the reverse scheme, convergence was always achieved which enabled ever increasing time increments. In contrast the time increments required for convergence were limited for calculations using the forward scheme.

The lower convergence rate with increase in the number of active slip systems (from 1D to 3D) was an important observation which led to the development of a hybrid scheme. As shown in Section 4.4, the reverse scheme has a relatively high convergence rate in the first part of the solution where error is highest, which then rapidly decreases once the error is below $\sim$50 to 150 MPa. The hybrid scheme first uses the reverse scheme to progress the solution to within the interval of convergence for the forward scheme and then transitions to the forward scheme with a higher convergence rate. To the authors' knowledge, the use of a hybrid approach that utilises both reverse and forward schemes, and thus takes advantage of superior robustness and efficiency at different parts within the same pointwise solution is the first of its kind. The hybrid approach offers relatively convenient implementation into existing crystal plasticity code, since the reverse scheme solver can simply be included as a standalone subroutine or function, which is called prior to the pre-existing NR solver based on the forward scheme.

For all pointwise calculations presented in Section 4 and the CPFEM simulations of a plate with a hole, the forward scheme with an initial guess based on the previous stress exhibited relatively high convergence rates and successful convergence for large time increments. However, the strong performance was in part due to the constant stress post yield resulting from the elastic-perfectly plastic (no hardening) material model and the constant deformation rate used in this study. The cyclic loading and non-linear strain hardening used in the polycrystalline Zircaloy-4 model presented in Section 5.2 was an exception and demonstrates that an initial guess based on

previous stress does not perform as well for general applications. Despite this, the approach was shown to offer some improvements in convergence rate (by a factor of two) over the conventional forward scheme with a stress guess based on elastic increment; for future studies, a less convenient test for this method may involve application to a material with a more substantial rate of strain-hardening than Zircaloy-4, e.g., a TWIP steel (De Cooman, 2017). Overall, the hybrid solver was shown to perform up to four times as well as the forward scheme based on previous stress, and almost an order of magnitude greater than the forward scheme based on an elastic predictor. For all CPFEM simulations presented in Section 5, the maximum time increment for each simulation was predominantly limited by convergence failure of the CP solver when using the conventional forward scheme based on an elastic predictor; this limitation was significantly reduced when using the hybrid scheme with a low transition tolerance (e.g., $\zeta = 1.0$ MPa^{-1}) and convergence of the global equilibrium solver was more influential in simulation performance.

A constant strain rate and perfectly plastic material behavior is certainly not representative of real-life applications and materials, and as a result it is rarely encountered in crystal plasticity studies also. Locally, crystal plasticity problems can encounter instantaneous changes to boundary conditions due to contact problems, crack propagation or complex loading, and stochastic material behavior due to the influence of strain gradients, crack propagation, phase transformation or even dislocation source activation. These highly non-linear problems all increase the difficulty in solving crystal plasticity problems and ultimately increase the number of increments and computational resource required for simulations. The simulations presented in Section 5.2 demonstrated the performance of the hybrid solver for an engineering relevant, challenging problem that included cyclic loading of a polycrystal with both non-linear hardening and crack propagation. In this case the hybrid scheme reduced the number of increments by a factor of six to nine compared to the conventional forward scheme.

Given the similarity of all common slip laws used in crystal plasticity, where the slip rate increases more rapidly with increase in stress, inverted slip laws will have a similar form and the reverse scheme offers superior stability at high deformation rates as shown in Appendix B for the power type slip law and the enthalpy based slip law, and in the main text for the hyperbolic sine slip law. Given the specific limits and convergence behaviors of different slip laws, the relative stability of the reverse and forward schemes depends on the stress/strain rate conditions suggesting that the hybrid scheme may not always be the best method to exploit the added robustness offered by the reverse scheme. Instead, for the power and enthalpy based slip laws investigated in Appendix B, it is proposed that the most appropriate solver would first attempt a solution using the forward scheme, then uses the reverse scheme if the forwards scheme fails to converge.

In conclusion the reverse scheme can be implemented to offer improved simulation efficiency for a wide range of rate dependent CPFEM applications, it is general to models using all common slip laws and several other sources of non-linearity.

Authors' statement

All persons who meet authorship criteria are listed as authors, and all authors certify that they have participated sufficiently in the work to take public responsibility for the content, including participation in the concept, design, analysis, writing, or revision of the manuscript. Furthermore, each author certifies that this material or similar material has not been and will not be submitted to or published in any other publication before its appearance in the International Journal of Plasticity.

CRediT authorship contribution statement

Chris Hardie: Conceptualization, Methodology, Software, Validation, Formal analysis, Investigation, Data curation, Writing – original draft, Writing – review & editing, Visualization. **Daniel J. Long:** Formal analysis, Investigation, Writing – original draft, Writing – review & editing, Visualization. **Eralp Demir:** Software, Writing – review & editing. **Edmund Tarleton:** Writing – review & editing. **Fionn P.E. Dunne:** Writing – review & editing, Supervision.

Declaration of Competing Interest

The authors declare that they have no known competing financial interests or personal relationships that could have appeared to influence the work reported in this paper.

Data availability

Data will be made available on request.

Acknowledgments

The authors gratefully acknowledge the review and technical discussions from Dr David Foster at UK Atomic Energy Authority. E. Tarleton acknowledges financial support from the Royal Academy of Engineering through a Senior Research Fellowship.

Appendix A. Slip systems in FCC copper

The slip systems definitions with plane normal and directions used in this study are shown in Fig. 14 (Lu et al., 2020).

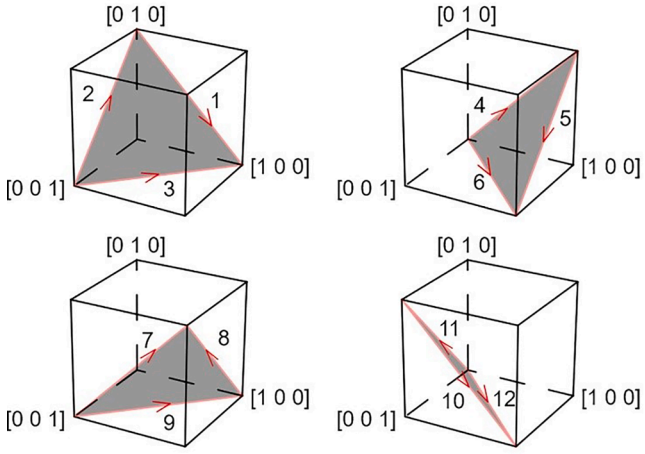

Slip System	Slip Plane, n	Slip Direction, s
1	(1 1 1)	[1 $\bar{1}$ 0]
2	(1 1 1)	[0 1 $\bar{1}$]
3	(1 1 1)	[1 0 $\bar{1}$]
4	($\bar{1}$ 1 1)	[1 1 0]
5	($\bar{1}$ 1 1)	[0 1 $\bar{1}$]
6	($\bar{1}$ 1 1)	[1 0 1]
7	(1 $\bar{1}$ 1)	[1 1 0]
8	(1 $\bar{1}$ 1)	[0 1 1]
9	(1 $\bar{1}$ 1)	[1 0 $\bar{1}$]
10	(1 1 $\bar{1}$)	[1 $\bar{1}$ 0]
11	(1 1 $\bar{1}$)	[0 1 1]
12	(1 1 $\bar{1}$)	[1 0 1]

Fig. 14. FCC slip system definitions used in this study. The table shows the slip system plane normal and slip directions with respect to orthogonal (x, y, z) reference coordinates. Figure taken from Lu et al. (2020).

Appendix B. Applicability to other common slip laws

This appendix introduces the formulae and results for pointwise calculations in three dimensions using two additional slip laws, i.e., the power type slip law and the enthalpy based slip law first introduced by Kocks et al. (1975), which are the only other slip laws commonly used and reported on in the literature.

The power law (equivalent to Eq. (9) in the main text) is:

$$\dot{\gamma}^k_{\mathrm{p}} = \dot{\gamma}_0 \left(\frac{|\tau^k|}{\tau^k_{\mathrm{c}}} \right)^m \mathrm{sgn}\left(\tau^k\right) \tag{39}$$

which in it's inverted form (equivalent to Eq. (16)) is:

$$\tau^k_{\mathrm{vp}} = \tau^k_{\mathrm{c}} \left(\frac{|\dot{\gamma}^k|}{\dot{\gamma}_0} \right)^{\frac{1}{m}} \mathrm{sgn}\left(\dot{\gamma}^k_{\mathrm{p}}\right) \tag{40}$$

where $\dot{\gamma}_0$ is the reference shear rate and m is the power law exponent, where $m > 1$ and typically $10 < m < 100$.

The derivatives of both with respect to the free variable are:

$$\frac{d\dot{\gamma}^k_{\mathrm{p}}}{d\tau^k} = \frac{m\dot{\gamma}_0}{\tau^k_{\mathrm{c}}} \left(\frac{|\tau^k|}{\tau^k_{\mathrm{c}}} \right)^{m-1} \tag{41}$$

for the forward case and

$$\frac{d\tau^k_{\mathrm{vp}}}{d\dot{\gamma}^k_{\mathrm{p}}} = \frac{\tau^k_{\mathrm{c}}}{m\dot{\gamma}_0} \left(\frac{|\dot{\gamma}^k|}{\dot{\gamma}_0} \right)^{\frac{1-m}{m}} \text{ for } |\dot{\gamma}^k| > 0 \tag{42}$$

for the inverted case, which are equivalent to Eqs. (15) and 17 in the main text respectively. It should be noted here that this slip law is a continuous function, without bounds in τ^k. The calculations were based on FCC copper, with $\tau^k_{\mathrm{c}} = 32$ MPa, $\dot{\gamma}_0 = 10^{-9}$ s^{-1} and $m = 13$ as taken from Wang et al. (2018). The value of the power law exponent is quite typical for metals and the exponent in Eq. (42) is negative, hence the non-zero condition on slip rate. Given that stability of the reverse scheme relies on conditioning with an initial guess of zero slip rate, $\frac{d\tau^k_{\mathrm{vp}}}{d\dot{\gamma}^k_{\mathrm{p}}} = 0$ MPa s was defined when $|\dot{\gamma}^k| = 0$ s^{-1}.

Identical calculations to those described in Section 4.3, i.e., for multiple slip systems in three dimensions, were carried out using the above slip law and parameters. The results for the maximum time increment and corresponding number of iterations required for convergence is given in Table 6. Due a higher τ^k_{c} compared to that used in the main text, the material response was effectively fully elastic for condition A. The forward schemes failed to solve for uni-axial loading with conditions B and C, where the solvable time

increment progressed to smaller than 10^{-90} s and the calculation was manually terminated. In contrast the reverse solver successfully converged both higher deformation rates for the uni-axial case, however the scheme failed to converge for the case of shear loading under condition B. This was due to instability, which was mitigated by changing χ from 2.0 to 0.1 in Eq. (28) which defined the step size; this resulted in progressively increasing time increments with the largest 0.3375 s increment requiring 2024 iterations.

The enthalpy based slip law is:

$$\dot{\gamma}_{\mathrm{p}}^{k} = \dot{\gamma}_0 \exp\left(-\frac{Q}{k_B T}\left[1 - \left(\frac{|\tau^k| - \tau_{\mathrm{c\_a}}^k}{\tau_{\mathrm{c\_t}}^k}\right)^p\right]^q\right)\mathrm{sgn}\left(\tau^k\right) \tag{43}$$

which in it's inverted form is:

$$\tau_{\mathrm{vp}}^{k} = \left(\tau_{\mathrm{c\_a}}^k + \tau_{\mathrm{c\_t}}^k\left[1 - u^{\frac{1}{q}}\right]^{\frac{1}{p}}\right)\mathrm{sgn}\left(\dot{\gamma}_{\mathrm{p}}^k\right) \tag{44}$$

where:

$$u = -\ln\left(\frac{|\dot{\gamma}^k|}{\dot{\gamma}_0}\right)\ \frac{k_B T}{Q} \tag{45}$$

and Q is the activation energy, k_B is the Boltzmann constant, T is the temperature, p and q are fitting parameters, and $\tau_{\mathrm{c\_a}}^k$ and $\tau_{\mathrm{c\_t}}^k$ are the athermal and thermal resistances to slip respectively. The derivatives of Eq. (43) with respect to shear stresses solved in the forward case is:

$$\frac{d\dot{\gamma}_{\mathrm{p}}^k}{d\tau^k} = \frac{|\dot{\gamma}^k| Qqp}{k_B T \tau_{\mathrm{c\_t}}^k}\left[1 - \left(\frac{|\tau^k| - \tau_{\mathrm{c\_a}}^k}{\tau_{\mathrm{c\_t}}^k}\right)^p\right]^{q-1}\left(\frac{|\tau^k| - \tau_{\mathrm{c\_a}}^k}{\tau_{\mathrm{c\_t}}^k}\right)^{p-1} \tag{46}$$

and the derivative of Eq. (44) with respect to the slip rates solved in the reverse case is:

$$\frac{d\tau_{\mathrm{vp}}^k}{d\dot{\gamma}_{\mathrm{p}}^k} = \frac{k_B T \tau_{\mathrm{c\_t}}^k}{|\dot{\gamma}^k| Qqp}\left[1 - u^{\frac{1}{q}}\right]^{\frac{1-p}{p}} u^{\frac{1-q}{q}} \text{ for } |\dot{\gamma}^k| > 0 \tag{47}$$

As the case for the power law, $\frac{d\tau_{\mathrm{vp}}^k}{d\dot{\gamma}_{\mathrm{p}}^k} = 0$ MPas was defined when $|\dot{\gamma}^k| = 0\ \mathrm{s}^{-1}$. For the calculations using the enthalpy based slip law, $Q = 2.77 \times 10^{-19}$ J, $T = 293$ K, $q = 1.2$, $p = 0.2$, and $\tau_{\mathrm{c\_t}}^k = 6.0$ MPa as taken from Lu et al. (2019). To support comparison with results presented in the main text and to facilitate the deformation rates studied, $\tau_{\mathrm{c\_a}}^k = 1.0$ MPa and $\dot{\gamma}_0 = 1.4\ \mathrm{s}^{-1}$. This deviation from the parameters given in Lu et al. (2019) was required due to the limits imposed by the enthalpy based slip law, which are $|\tau^k| \leq \tau_{\mathrm{c\_a}}^k + \tau_{\mathrm{c\_t}}^k$ and $\dot{\gamma}_0 \exp\left(-\frac{Q}{k_B T}\right) < |\dot{\gamma}^k| \leq \dot{\gamma}_0$. Not only does this limit the applicability of the enthalpy based slip law, more importantly in the context of this work it imposes an additional limit to the upper bound of the interval of convergence.

Again, identical calculations to those described Section 4.3 were carried out using the enthalpy based slip law and the results are shown in Table 7. These results are like those for the power law, where the time increment in the forward scheme progressively decreased for condition C when using the initial guess based on an elastic increment and the calculation was manually terminated. The reverse scheme was unstable for shear loading under condition A and subsequent investigation showed that like the power law, $\chi = 0.1$ was required for stability, resulting in progressively increasing time increments with the largest 0.3375 s increment requiring 1664 iterations.

The calculations conducted as part of this study, suggest that the use of the hybrid scheme with the power and enthalpy based slip laws investigated above is less appropriate due to the different convergence rates these two slip laws exhibited for the reverse scheme and the lack of stability in the reverse scheme for lower deformation rates in some cases. The reverse scheme was shown to offer superior robustness for higher deformation rates, where the forward scheme failed, whilst the forward scheme had higher convergence rates where it was successful. Given that no single scheme successfully solved all loading types and conditions investigated, yet all were solved when applying both schemes, it is likely that significant improvement of performance for CPFEM calculations can be found by using both schemes separately. Due to the superior convergence rate and fail fast nature of the forward scheme initiated with a guess based on previous stress, this should be used first, followed by application of the reverse scheme when convergence fails using the forward scheme.

Table 6
Maximum time increment (in parentheses) and corresponding number of iterations required for convergence, for both loading types and deformation rate conditions A, B and C and for each calculation method using the power law.

No. of iterations for increment (max Δt, s)			
Uni-axial Loading	Condition A	Condition B	Condition C
Reverse Scheme	Fully Elastic	32 (0.3375)	37 (0.3375)
Forward Scheme - Elastic Increment		FAILED ($<10^{-90}$)	FAILED ($<10^{-90}$)
Forward Scheme - Previous Stress		FAILED ($<10^{-90}$)	FAILED ($<10^{-90}$)
Shear Loading	Condition A	Condition B	Condition C
Reverse Scheme	Fully Elastic	FAILED	1006 (0.3375)
Forward Scheme - Elastic Increment		14 (0.1688)	8 (0.0031)
Forward Scheme - Previous Stress		5 (0.3375)	26 (0.1802)

Table 7
Maximum time increment (in parentheses) and corresponding number of iterations required for convergence, for both loading types and deformation rate conditions A, B and C and for each calculation method using the enthalpy based slip law.

No. of iterations for increment (max Δt, s)			
Uni-axial Loading	Condition A	Condition B	Condition C
Reverse Scheme	28 (0.3375)	31 (0.3375)	37 (0.3375)
Forward Scheme - Elastic Increment	13 (0.1125)	6 (0.0031)	FAILED ($\sim 10^{-7}$)
Forward Scheme - Previous Stress	3 (0.3375)	1 (0.2703)	1 (0.3082)
Shear Loading	Condition A	Condition B	Condition C
Reverse Scheme	FAILED	420 (0.3375)	34846 (0.3375)
Forward Scheme - Elastic Increment	13 (0.2531)	5 (0.0063)	FAILED ($\sim 10^{-7}$)
Forward Scheme - Previous Stress	4 (0.3375)	2 (0.2917)	4 (0.2740)

References

Akpama, H.K., Bettaieb, M.Ben, Abed-Meraim, F., 2016. Numerical integration of rate-independent BCC single crystal plasticity models: comparative study of two classes of numerical algorithms. Int. J. Numer. Methods Eng. 108, 363–422. https://doi.org/10.1002/nme.5215.

Belytschko, T., Black, T., 1999. Elastic crack growth in finite elements with minimal remeshing. Int. J. Numer. Methods Eng. 45, 601–620. https://doi.org/10.1002/(SICI)1097-0207(19990620)45:5<601::AID-NME598>3.0.CO;2-S.

Busso, E.P., Cailletaud, G., 2005. On the selection of active slip systems in crystal plasticity. Int. J. Plast. 21, 2212–2231. https://doi.org/10.1016/J.IJPLAS.2005.03.019.

Cackett, A.J., Hardie, C.D., Lim, J.J.H., Tarleton, E., 2019. Spherical indentation of copper: crystal plasticity vs experiment. Materialia 7. https://doi.org/10.1016/j.mtla.2019.100368 (Oxf).

Cuitino, A.M., Ortiz, M., 1993. Computational modelling of single crystals. Model. Simul. Mater. Sci. Eng. 1, 225. https://doi.org/10.1088/0965-0393/1/3/001.

Dadhich, R., Alankar, A., 2022. A modular spectral solver for crystal plasticity. Int. J. Plast. 156, 103328 https://doi.org/10.1016/j.ijplas.2022.103328.

De Cooman, B.C., 2017. High Mn TWIP steel and medium Mn steel. Automotive Steels: Design, Metallurgy, Processing and Applications 317–385. https://doi.org/10.1016/B978-0-08-100638-2.00011-0.

Dumoulin, S., Hopperstad, O.S., Berstad, T., 2009. Investigation of integration algorithms for rate-dependent crystal plasticity using explicit finite element codes. Comput. Mater. Sci. 46, 785–799. https://doi.org/10.1016/j.commatsci.2009.04.015.

Dunne, F.P.E., Rugg, D., Walker, A., 2007. Lengthscale-dependent, elastically anisotropic, physically-based hcp crystal plasticity: application to cold-dwell fatigue in Ti alloys. Int. J. Plast. 23, 1061–1083. https://doi.org/10.1016/J.IJPLAS.2006.10.013.

Hardie, C., Thomas, R., Liu, Y., Frankel, P., Dunne, F., 2022. Simulation of crystal plasticity in irradiated metals: a case study on Zircaloy-4. Acta Mater. 241 https://doi.org/10.1016/j.actamat.2022.118361.

Harewood, F.J., McHugh, P.E., 2007. Comparison of the implicit and explicit finite element methods using crystal plasticity. Comput. Mater. Sci. 39, 481–494. https://doi.org/10.1016/j.commatsci.2006.08.002.

Huang, Y., 1991. A user-material subroutine incorporating single crystal plasticity in the ABAQUS finite element program (Masters Thesis). Harvard University, Cambridge.

Kocks, U.F., Argon, A.S., Ashby, M., 1975. Thermodynamics and kinetics of slip. Prog Mater Sci 19, 110–170. https://doi.org/10.1016/0079-6425(75)90005-5.

Lebensohn, R.A., Needleman, A., 2016. Numerical implementation of non-local polycrystal plasticity using fast Fourier transforms. J. Mech. Phys. Solids 97, 333–351. https://doi.org/10.1016/j.jmps.2016.03.023.

Ling, X., Horstemeyer, M.F., Potirniche, G.P., 2005. On the numerical implementation of 3D rate-dependent single crystal plasticity formulations. Int. J. Numer. Methods Eng. 63, 548–568. https://doi.org/10.1002/nme.1289.

Liu, Y., Wan, W., Dunne, F.P.E., 2022. Characterisation and modelling of micro- and macroscale creep and strain rate sensitivity in Zircaloy-4. Mater. Sci. Eng. A 840, 142981. https://doi.org/10.1016/J.MSEA.2022.142981.

Lu, X., Dunne, F.P.E., Xu, Y., 2020. A crystal plasticity investigation of slip system interaction, GND density and stored energy in non-proportional fatigue in Nickel-based superalloy. Int. J. Fatigue 139, 105782. https://doi.org/10.1016/J.IJFATIGUE.2020.105782.

Lu, X., Zhang, X., Shi, M., Roters, F., Kang, G., Raabe, D., 2019. Dislocation mechanism based size-dependent crystal plasticity modeling and simulation of gradient nano-grained copper. Int. J. Plast. 113, 52–73. https://doi.org/10.1016/j.ijplas.2018.09.007.

Mánik, T., Asadkandi, H.M., Holmedal, B., 2022. A robust algorithm for rate-independent crystal plasticity. Comput. Methods Appl. Mech. Eng. 393, 114831 https://doi.org/10.1016/J.CMA.2022.114831.

McGinty, R.D., 2001. Multiscale Representation of Polycrystalline Inelasticity (PhD Thesis). Georgia Institute of Technology.

Miehe, C., Schröder, J., 2001. Comparative study of stress update algorithms for rate-independent and rate-dependent crystal plasticity. Int. J. Numer. Methods Eng. 50, 273–298. https://doi.org/10.1002/1097-0207(20010120)50:2<273::AID-NME17>3.0.CO;2-Q.

Peirce, D., Asaro, R.J., Needleman, A., 1983. Material rate dependence and localized deformation in crystalline solids. Acta Metall. 31, 1951–1976. https://doi.org/10.1016/0001-6160(83)90014-7.

Roters, F., Diehl, M., Shanthraj, P., Eisenlohr, P., Reuber, C., Wong, S.L., Maiti, T., Ebrahimi, A., Hochrainer, T., Fabritius, H.O., Nikolov, S., Friák, M., Fujita, N., Grilli, N., Janssens, K.G.F., Jia, N., Kok, P.J.J., Ma, D., Meier, F., Werner, E., Stricker, M., Weygand, D., Raabe, D., 2019. DAMASK – The Düsseldorf advanced material simulation kit for modeling multi-physics crystal plasticity, thermal, and damage phenomena from the single crystal up to the component scale. Comput. Mater. Sci. 158, 420–478. https://doi.org/10.1016/J.COMMATSCI.2018.04.030.

Roters, F., Eisenlohr, P., Hantcherli, L., Tjahjanto, D.D., Bieler, T.R., Raabe, D., 2010. Overview of constitutive laws, kinematics, homogenization and multiscale methods in crystal plasticity finite-element modeling: theory, experiments, applications. Acta Mater. 58, 1152–1211. https://doi.org/10.1016/j.actamat.2009.10.058.

Thomas, R., Lunt, D., Atkinson, M.D., Quinta da Fonseca, J., Preuss, M., Barton, F., O'Hanlon, J., Frankel, P., 2019. Characterisation of irradiation enhanced strain localisation in a zirconium alloy. Materialia 5, 100248. https://doi.org/10.1016/j.mtla.2019.100248 (Oxf).

Vieira de Carvalho, M., Cardoso Coelho, R.P., Pires, F.M.A., 2022. On the computational treatment of fully coupled crystal plasticity slip and martensitic transformation constitutive models at finite strains. Int. J. Numer. Methods Eng. 123, 5155–5200. https://doi.org/10.1002/NME.7059.

Wang, Z., Zhang, Junjie, Hassan, H.ul, Zhang, Jianguo, Yan, Y., Hartmaier, A., Sun, T., 2018. Coupled effect of crystallographic orientation and indenter geometry on nanoindentation of single crystalline copper. Int. J. Mech. Sci. 148, 531–539. https://doi.org/10.1016/j.ijmecsci.2018.09.007.

Wilson, D., Dunne, F.P.E., 2019. A mechanistic modelling methodology for microstructure-sensitive fatigue crack growth. J. Mech. Phys. Solids 124, 827–848. https://doi.org/10.1016/j.jmps.2018.11.023.

Wilson, D., Zheng, Z., Dunne, F.P.E., 2018. A microstructure-sensitive driving force for crack growth. J. Mech. Phys. Solids 121, 147–174. https://doi.org/10.1016/j.jmps.2018.07.005.

Wisner, S.B., Reynolds, M.B., Adamson, R.B., 1994. Fatigue Behavior of Irradiated and Unirradiated Zircaloy and Zirconium. ASTM Special Technical Publication, pp. 499–520. STP15206S.

Xu, Y., Wan, W., Dunne, F.P.E., 2021. Microstructural fracture mechanics: stored energy density at fatigue cracks. J. Mech. Phys. Solids 146. https://doi.org/10.1016/j.jmps.2020.104209.

Zhang, P., Zhang, L., Baxevanakis, K.P., Zhao, L.G., Bullough, C., 2020. Modelling short crack propagation in a single crystal nickel-based superalloy using crystal plasticity and XFEM. Int. J. Fatigue 136, 105594. https://doi.org/10.1016/j.ijfatigue.2020.105594.

Zhao, N., Roy, A., Wang, W., Zhao, L., Silberschmidt, V.V., 2019. Coupling crystal plasticity and continuum damage mechanics for creep assessment in Cr-based power-plant steel. Mech. Mater. 130, 29–38. https://doi.org/10.1016/J.MECHMAT.2019.01.006.